

Similarity Metrics for MR Image-to-Image Translation

Melanie Dohmen¹, Mark Klemens¹, Ivo Baltruschat¹, Tuan Truong¹, and Matthias Lengua¹

¹Bayer AG, Radiology, Berlin, Germany
firstname.lastname@bayer.com

ABSTRACT

Image-to-image translation can create large impact in medical imaging, for instance the possibility to synthetically transform images to other modalities, sequence types, higher resolutions or lower noise levels. In order to assure a high level of patient safety, these methods are mostly validated by human reader studies, which require a considerable amount of time and costs. Quantitative metrics have been used to complement such studies and to provide reproducible and objective assessment of synthetic images. Even though the SSIM and PSNR metrics are extensively used, they do not detect all types of errors in synthetic images as desired. Other metrics could provide additional useful evaluation.

In this study, we give an overview and a quantitative analysis of 15 metrics for assessing the quality of synthetically generated images. We include 11 full-reference metrics (SSIM, MS-SSIM, CW-SSIM, PSNR, MSE, NMSE, MAE, LPIPS, DISTs, NMI and PCC), three non-reference metrics (BLUR, MLC, MSLC) and one downstream task segmentation metric (DICE) to detect 11 kinds of typical distortions and artifacts that occur in MR images. In addition, we analyze the influence of four prominent normalization methods (Minmax, cMinmax, Zscore and Quantile) on the different metrics and distortions. Finally, we provide adverse examples to highlight pitfalls in metric assessment and derive recommendations for effective usage of the analyzed similarity metrics for evaluation of image-to-image translation models.

1 Introduction

Recent advances in generative artificial intelligence (AI) within the natural image domain have demonstrated a remarkable capability to produce synthetic images with high fidelity, capturing nuances such as lighting variations, textures, and object placements^{1,2}. These approaches typically rely on neural network architectures and the availability of large-scale datasets. One of the key techniques that have contributed to this capability are Generative Adversarial Networks (GANs)³. In GANs, a generator network learns to produce synthetic images that are then evaluated by a discriminator network, which distinguishes between real and synthetic images. Through this adversarial process, both networks iteratively improve, leading to the generation of increasingly realistic images. Other approaches for image synthesis rely on Variational Autoencoders (VAEs)^{4,5}, a class of generative models, consisting of two main components: an encoder and a decoder. The encoder network maps input images into a lower-dimensional latent space, where each point represents a latent code encoding important features of the input image. This latent representation captures the underlying structure and variability of the data. The decoder network then takes samples from the latent space and reconstructs them back into the original input space, generating synthetic images. In addition to traditional approaches like GANs and VAEs, a recent breakthrough in the field of generative artificial intelligence comes from diffusion models⁶. Unlike GANs, which operate through an adversarial training scheme, diffusion models follow a different paradigm inspired by the process of diffusion in physics. These models iteratively transform a simple noise distribution into complex data distributions, such as natural images, by gradually reducing noise to the input data. Furthermore, by combining the strengths of different generative approaches, improving neural network optimization, and the increasing availability of computing resources, researchers are continuing to advance the field of synthetic image generation. The implications of these advancements are far-reaching, with applications spanning various domains such as computer vision, graphics, augmented and virtual reality, or creative arts. Still, many challenges remain, including the potential for biases in generated images, the need for improved diversity and controllability in generation, and ethical considerations surrounding the use of AI-generated content.

1.1 Image Synthesis in Medical Imaging

The adaption of novel generative modeling concepts to the medical imaging domain is being explored with continuously growing interest and many relevant use cases have been already identified. For training deep neural networks, typically very large and diverse data sets are needed, but these are rarely available for medical imaging tasks. Generative networks can amend available data with synthetic samples and thereby improve the performance of other image analysis tasks⁷. Another line of research develops conditional generative models for image-to-image translation, which aims to translate a given image to a synthetic output image, showing the same content (e.g. patient, organ or biological sample) as the input but with a different appearance (e.g. contrasting structures differently, changing texture or resolution). Input and output typically belong to different

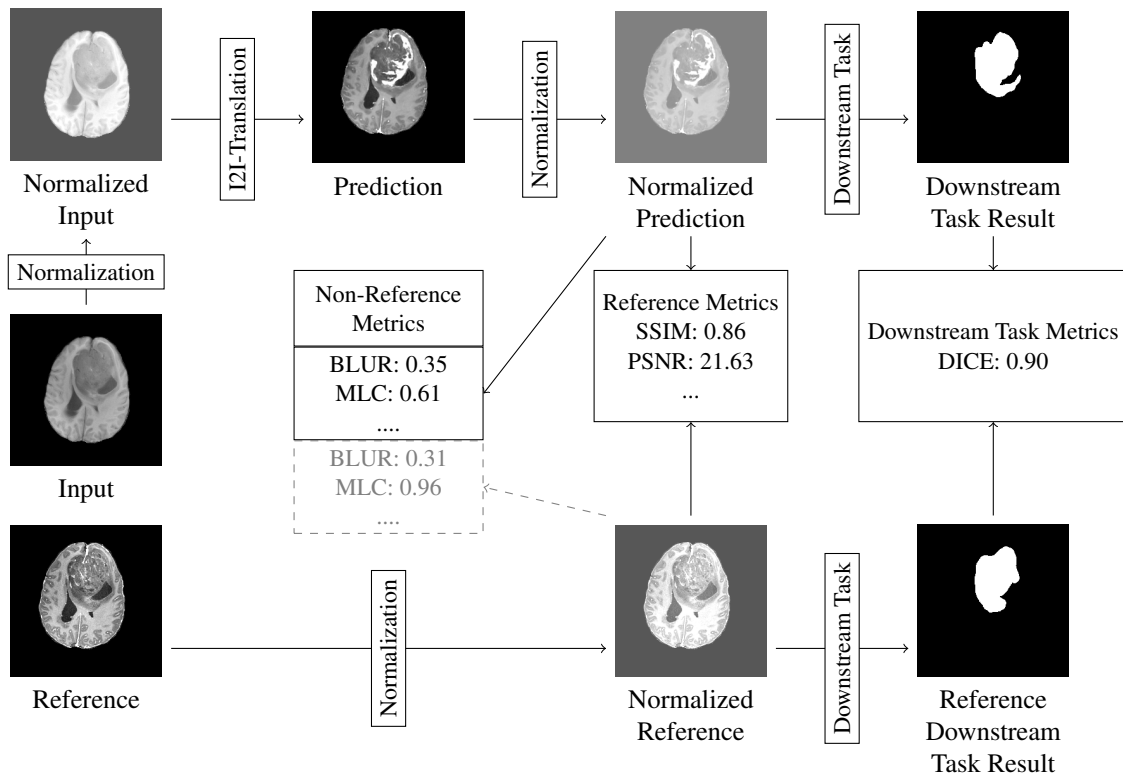


Figure 1. Overview of Image-To-Image Translation and Validation. Given an input image, it is typically normalized before being translated to a prediction in the target domain. If a reference image is given, this also belongs to the target domain. To make sure, prediction and reference are comparable, both should be normalized to a common scale. Then there are multiple possibilities to apply metrics. Reference metrics directly compare normalized prediction and normalized reference image. Non-reference metrics can be applied to the normalized prediction alone, but also -if available - to a predicted normalized reference. Then both non-reference metric scores can be compared. Third, the normalized reference and the normalized prediction can be further processed in a downstream task, i.e. a segmentation task. The performance of both downstream task results is then assessed with a downstream task metric, i.e. a segmentation metric.

image domains. The input domain is referred to as **source** domain, while the output belongs to a **target** domain. Depending on the availability of source and target pairs of the same patient or structure in the training data, image-to-image translation can be performed in a paired manner, also referred to as supervised². Otherwise, unpaired⁸, also called unsupervised, image-to-image translation aims to learn how to transfer characteristics from the entire target domain to a specific input image from the source domain. These tasks are specifically interesting in medicine⁹, because they allow to translate a medical image from one domain to another. Source and target domain may differ by imaging modality or acquisition parameters, such that image-to-image translation allows translation, e.g., from computed tomography (CT) to magnetic resonance (MR) imaging¹⁰ or vice-versa, from T1-weighted MR to T2-weighted MR¹¹, CT to positron emission tomography (PET)¹², PET to CT¹³, or from native MR to contrast-enhanced MR¹⁴. When the source image acquisition is less harmful, acquired faster, cheaper, or already existent, while the target image is preferred for diagnosis and may be more harmful, more expensive, more time-consuming, or simply not available, a large benefit for the patient is possible. For example, radiation dose, invasive or painful examinations can be reduced or even avoided. Low-quality or low-resolution images can be restored, improved, or the resolution increased¹⁵. For radiation therapy, which is planned based on CT images, MR to CT synthesis has been investigated¹⁶. MR to CT synthesis is also used for facilitating registration between both modalities¹⁷. The translation between different MR-sequences (T1-weighted, T2-weighted, T2-FLAIR) can complete the missing series for improved diagnosis¹⁸. For reducing patient burden with contrast agents, researchers work on the translation of native or low-dose MR images to synthetic high contrast-enhanced images¹⁹.

1.2 Validation Metrics for Image Synthesis

However, validation of these approaches is not straightforward. Besides manual evaluation by humans, metrics assessing a whole distribution of synthesized images are most popular for evaluating GANs²⁰, i.e. the Inception Score²¹ or the Fréchet

Inception Distance²². These metrics aim to assess the diversity of the generated images and the coverage and similarity to a reference set of images. Another group called (full-) **reference metrics** assesses the similarity between two images. In the context of image synthesis, one image is synthesized and it is then compared to a reference image, representing a desired synthesis result. For this validation setup, a dataset with input and target pairs is needed. Synthesis models leveraging such data are often referred to as paired or supervised image-to-image translation models. A third group of metrics, referred to as **non-reference metrics** or quality metrics, assesses the quality of a single image. As quality requirements may vary between tasks and image domains, metrics for different aspects have been developed, e.g. for measuring blurriness²³, contrast²⁴ or other features inspired by human perception²⁵.

Slight spatial misalignment between paired images remains a problem for evaluation with reference metrics, such that specialized methods have been investigated for this purpose. By assessing similarity in the complex-wavelet domain, complex-wavelet SSIM (CW-SSIM) is able to ignore small translations, scaling and rotations²⁶. A Score derived from features of the Segment Anything Model (SAM), mainly compares semantic features and therefore better ignores different style and small deformations²⁷. The learned Deep Image Structure and Texture Similarity (DISTS) metric gives more weight to texture similarity, ignoring fine-grained misalignment of these textures²⁸.

In the domain of natural images, reference metrics have been extensively tested on synthetically distorted images. The Tampere Image Database²⁹ contains 25 reference images with 17 types of distortions in four strength levels, which were randomly paired and presented to human for qualitative comparison. Derived from a tournament scoring system, mean opinion scores in the range [0, 9] were derived. The LIVE Image Quality Assessment Database^{30,31} contains 29 reference images and 779 distorted images of five distortion types. The quality of these images was rated manually by many readers in the range [1, 5] and differential mean opinion scores (DMOS) were derived in the range [0, 100]. Spearman and Kendall rank correlation between different reference metrics and MOS or DMOS were used to measure which metrics best correspond to human perception. However, these results cannot be fully transferred to medical image synthesis. Even though a similar study for MR images³² exists, we doubt that the majority of included distortions, such as JPEG compression artifacts and white noise, are relevant for medical image synthesis. Instead, MR imaging exhibits very specific acquisition artifacts, such as bias field, ghosting or stripe artifacts. Additionally, certain synthesis models may introduce other kinds of distortions, e.g. the insertion of artificial structures or registration artifacts that arise from misaligned source and target images. In this study, we create a similar benchmark dataset for the medical images domain consisting of 100 MR reference images and 11 distortions in 5 strengths. Instead of MOS scores, which were not possible to collect in such a large number for this study, we calibrated the distortion strengths manually to approximately generate similar quality images among distortions of the same strength. This allows to compare different metrics regarding their sensitivity towards each kind of distortion. We also argue for considering each distortion by itself instead of averaging over a fixed group of distortions, because the importance and appearance of single distortions may vary largely between different applications.

1.3 Validation in the Medical Domain

Even though human assessment will remain essential for validation in the medical image domain, it is also extremely costly, as it has to be performed by domain experts. Additionally, humans assess quality subjectively and non-reproducibly. Therefore, automatic quantitative assessment with metrics is a core part of validation, where reference metrics, non-reference metrics, and evaluation of downstream tasks are most prevalent^{33,34}.

Among 13 papers on image-to-image translation with generative adversarial networks (GANs) or convolutional neural networks (CNNs) in the medical domain³⁵, 84% use the structural similarity index measure (SSIM), and 61% use the peak signal-to-noise ratio (PSNR) for validation. A further review on synthetic contrast-enhancement of MR images³⁶ reports evaluation by SSIM and PSNR in 75% of the studies. Even though SSIM is known to underestimate blurriness³⁷ and PSNR is known to not correlate well with human perception³⁸, these shortcomings are often not appropriately accounted for. A huge amount of additional metrics has been used³⁵ to complement SSIM and PSNR. However, guidelines and consensus about which metrics are most appropriate for evaluating image synthesis in the medical domain seem to be missing. This validation gap is also reflected in the decreasing number of approved medical software devices with machine learning or artificial intelligence. While the number of such devices increased by 39% in 2020, the Food and Drug Administration in the United States reported an increase of only 15% and 14% in 2021 and 2022³⁹. For segmentation and classification tasks, there are already guidelines and studies to support the selection of appropriate metrics^{40,41}. By performing downstream tasks with synthesized images, such as segmentation or classification, these metrics can also be leveraged for validation of image synthesis⁴².

The workflow of image-to-image translation and the three types of validation metrics investigated in this study are shown in Fig. 1.

1.4 Contribution

In this paper, we provide a comprehensive overview and description of 11 reference metrics that can be used for image synthesis evaluation in the medical domain (see Sec. 2). To complement validation with reference metrics, we present suitable

non-reference metrics and exemplarily discuss the value of downstream task evaluation with a segmentation metric. In the experiments in Sec. 3, we systematically assess the sensitivity of nine reference and three non-reference metrics regarding 11 different distortions, that we assume to appear in MR image synthesis. Furthermore, we use three normalization methods before metric assessment and investigate their influence. Thereby, we aim to guide researchers in the appropriate selection of metrics for any desired synthesis task. Derived from the distortion experiment results in Sec. 4, we provide a set of adverse examples in Sec. 5, to showcase unexpected behaviour of the analyzed metrics. Finally, we discuss the behaviour of the metrics in the experiments in Sec. 6 and suggest recommendations for the validation of image-to-image translation methods specifically for MR image synthesis in Sec. 7.

2 Normalization and Metric Overview

In this section, we give an overview of reference and non-reference metrics for assessing the quality of images. Especially reference metrics strongly depend on intensity value ranges. Therefore, we first introduce normalization methods that are frequently used to bring MR images to a common intensity value scale.

2.1 Notation

Let I be an image with intensity $I(\mathbf{x})$ at pixel location \mathbf{x} . A three-dimensional image $I \in \mathbb{R}^{h \times w \times d}$ of height h , width w and depth d consists of $|I| = h \cdot w \cdot d$ pixels, with pixel locations denoted as $\mathbf{x} = (x_1, x_2, x_3) \in \mathbb{N}^3$ with $0 \leq x_1 < h$, $0 \leq x_2 < w$, $0 \leq x_3 < d$. Accordingly, a two-dimensional image is defined as $I \in \mathbb{R}^{h \times w}$ with pixel locations $\mathbf{x} = (x_1, x_2)$ and $|I| = h \cdot w$ pixels in total. Let I_{\max} denote the maximum intensity, I_{\min} the minimum intensity, μ_I the mean intensity, σ_I the standard deviation of all image intensities in I . The k -th percentile $I_{k\%} \in \mathbb{R}$ of the image I is the smallest intensity value, such that a fraction of $k\%$ of all pixels in I have lower or equal intensity value. The median of all image intensities in I is $I_{50\%}$. The interquartile range (IQR) is $I_{75\%} - I_{25\%}$.

Let I and R denote two images. In general, a reference metric M_r is a mapping that assigns a score $s \in \mathbb{R}$ to any tuple (I, R) , i.e. $M_r(I, R) = s$. A non-reference metric M_n is a mapping that assigns a score $s' \in \mathbb{R}$ to a single image input, i.e. $M_n(I) = s'$. A normalization function N is a mapping that transforms an input image by altering intensity values or even image size, i.e. $N(I) = I'$. Certain image normalization methods require parameters, that need to be previously determined from a whole set of input images.

2.2 Intensity Ranges, Data formats and Normalization Methods

Image normalization plays a crucial role in medical image processing, serving as a fundamental preprocessing step with significant implications for downstream processing, analysis, or the development of algorithms. Natural images are often acquired as RGB images with an 8-bit unsigned integer data format per channel, which corresponds to a value range of $[0, 255]$. Medical images, such as CT, MR, X-ray or ultra-sound may image exhibit much larger intensity ranges such as 12- to 16-bit unsigned integer or 32-bit floating point values. In addition, absolute intensity values may be differently scaled in qualitative imaging modalities such as MR, depending on scanner, software version or surrounding tissue. For these imaging modalities, normalization or standardization methods are needed for better quantitative comparison. For metrics, that were designed for 8-bit unsigned integer data format, adaptations to the metric or normalization to the images must be considered.

Normalization or standardization is not only needed as a prerequisite for metric assessment but is usually already performed as a preprocessing step for image-to-image translation. For deep-learning based methods, a reasonable and standardized scale such as $[-1, 1]$ or $[0, 1]$ is recommended⁴³. By modality specific normalization, deep-learning based models may even improve generalizability in case of heterogeneous input data sources^{44, 45}. Several normalization methods are used for MR images⁴⁶, which are typically acquired in a 16-bit integer format. Zscore normalization (see Section 2.2.2) and clipped Minmax normalization (see Section 2.2.1) have been applied before model training^{14, 47} to achieve numerical ranges near $[-1, 1]$ or strictly between $[0, 1]$, respectively. In addition, normalization methods have been developed for specifically for MR (piece-wise linear histogram matching⁴⁸) or even specifically for brain MR images (cf. WhiteStripe⁴⁹) in order to obtain quantitative comparable intensities for the same brain or body structures. The normalization methods investigated within this study are defined below, and an overview is shown in Tab.1.

2.2.1 Minmax and clipped Minmax

In the most general case, Minmax normalization shifts and scales a given (sub-) range $[i_{\min}, i_{\max}]$ of the image intensity values to a target intensity range $[j_{\min}, j_{\max}]$. For the most frequent choice of $i_{\min} = I_{\min}$, $i_{\max} = I_{\max}$, $j_{\min} = 0$ and $j_{\max} = 1$, these parameters can be dropped and the normalized image intensity range is completely transformed into the range $[0, 1]$ ⁴⁵.

$$\text{Minmax}_{i_{\min} \rightarrow j_{\min}, i_{\max} \rightarrow j_{\max}}(I) = \frac{I - i_{\min}}{i_{\max} - i_{\min}} \cdot (j_{\max} - j_{\min}) + j_{\min} \quad \text{Minmax}(I) = \frac{I - I_{\min}}{I_{\max} - I_{\min}} \quad (1)$$

Table 1. Overview of normalization methods. The methods with gray background are used in the experiments section. The target intensities j_{\min} and j_{\max} can be chosen arbitrarily, but are typically set to $[0, 1]$ or $[-1, 1]$.

Method	Description	Result range	References
Minmax	Shifts and scales image intensity values to a range with given minimum and maximum value.	$[j_{\min}, j_{\max}]$	45
cMinmax	Clips at lower and upper percentiles before Minmax. More robust to high and low outliers.	$[j_{\min}, j_{\max}]$	
Z-Score	Shifts the intensity values to a mean μ_I of 0 and scales to unit standard deviation σ_I .	$\mu_I = 0, \sigma_I = 1$	45
Quantile	Shifts the intensity values to a median of 0 and scales to a unit inter-quartile range (IQR = $I_{p75\%} - I_{p25\%}$).	median(I)=0, IQR=1	45
PL	Piecewise-Linear: The histogram is scaled linearly in two pieces to match three landmarks of a standard histogram derived from a set of reference images.	depends on reference dataset	48

Other variants of this normalization utilize quantiles instead of I_{\max} and I_{\min} , see 2.2.5 below. Clipped Minmax normalization¹⁴ is equal to Minmax normalization with previous clipping at the percentiles $I_{p\%}$ and $I_{q\%}$. Typically, the percentiles are chosen symmetrically, i.e. $p < 50\%$ and $q = 100\% - p$ and the output intensity range is set to $j_{\min} = 0$ and $j_{\max} = 1$ and the notation reduces to cMinmax $_{p\%}$. This normalization is less sensitive to outliers than Minmax, but reduces the total number of occurring intensity values and thereby removes some information.

$$\text{cMinmax}_{p\% \rightarrow j_{\min}, q\% \rightarrow j_{\max}}(I) = \text{Minmax}_{I_{p\%} \rightarrow j_{\min}, I_{q\%} \rightarrow j_{\max}}(\text{clip}_{I_{p\%}, I_{q\%}}(I)) \quad \text{clip}_{I_{p\%}, I_{q\%}}(I) = \begin{cases} I_{p\%} & , \text{ if } I(\mathbf{x}) \leq I_{p\%} \\ I_{q\%} & , \text{ if } I(\mathbf{x}) \geq I_{q\%} \\ I(\mathbf{x}) & , \text{ else} \end{cases} \quad (2)$$

$$\text{cMinmax}_{p\%}(I) = \text{Minmax}(\text{clip}_{I_{p\%}, I_{100\% - p\%}}(I))$$

2.2.2 Zscore

Zscore normalization⁴⁶ normalizes the mean and standard deviation of the intensity value distribution. To perform this normalization on an image, each pixel value is subtracted by μ_I and then divided by σ_I , i.e. the following transformation is applied:

$$\text{Zscore}(I) = \frac{I - \mu_I}{\sigma_I} \quad (3)$$

This results in an intensity value distribution with zero mean and unit standard deviation. This normalization technique brings pixel intensities to a standardized scale, and hence, the relative importance of different features within an image becomes more consistent, facilitating effective comparison and downstream analysis. In contrast to Minmax or cMinmax, the output value ranges, i.e. the minimum and maximum values, are not fixed and may differ after Zscore normalization.

2.2.3 Quantile

Quantile normalization⁴⁵, is similar to Zscore normalization, but utilizes the median $I_{50\%}$ instead of the mean, and the interquartile range instead of the standard deviation. Typically, it is therefore less biased by outliers in the image histogram. The following transformation is applied to all values of the image:

$$\text{Quantile}(I) = \frac{I - I_{50\%}}{I_{75\%} - I_{25\%}} \quad (4)$$

The resulting intensity value distribution has zero median and unit IQR. This normalization fails when $I_{25\%} = I_{75\%}$. In this case at least 50% of all pixels have the same intensity value. This may occur, where the constant image background is disproportionately large compared to the image foreground content.

2.2.4 Piece-wise linear standardization

In order to match histogram modes and minimum and maximum percentiles of an MR dataset showing the same body region, Nyul et al. introduced a piece-wise linear standardization procedure⁴⁸. The authors argue that for most body regions MR

images exhibit either a unimodal or a bimodal histogram, where the foreground concentrates around the only or the second mode respectively.

In a first step, a training set of J images I_j , $j \leq J$ is normalized with $\text{Minmax}_{I_j; p1\% \rightarrow s1, I_j; p2\% \rightarrow s2}(I_j) = I'_j$. Further, the first or second (in case of a bimodal histogram) mode $m_{I'_j}$, i.e. the most frequently occurring value in I'_j , is obtained for each normalized image I'_j . The $m_{I'_j}$ s are averaged to m_s . In the second step, any image I with mode m_I can be standardized with parameters $p1$, $p2$, $s1$, $s2$ and m_s . Values in $[I_{p1\%}, m_I]$ are shifted and scaled to range $[s1, m_s]$ and values from $[m_I, I_{p2\%}]$ are shifted and scaled to range $[m_s, s2]$. This yields histograms, that are linearly scaled in two segments to match the three mentioned landmarks: The lower $p1$ th percentile at $s1$, the (second) mode at m_s and the upper $p2$ th percentile at $s2$. A choice of $p1 = 0$ and $p2 = 99.8$ was suggested⁴⁸.

$$\text{PL}_{p1, p2, s1, s2, m_s}(I) = \begin{cases} \text{Minmax}_{I_{p1\%} \rightarrow s1, m_I \rightarrow m_s} & , \text{ if } I(\mathbf{x}) \leq m_I \\ \text{Minmax}_{m_I \rightarrow m_s, I_{p2\%} \rightarrow s2} & , \text{ else} \end{cases} \quad (5)$$

2.2.5 Region based estimation of normalization parameters

The transformation parameters of the aforementioned normalization techniques can also be estimated based on a region-of-interest (ROI) contained in the image. This typically requires a delineated ROI or at least a landmark. Common types of ROIs are the image foreground or a certain tissue type. For example, the WhiteStripe normalization⁴⁹ computes the mean μ_{WM} and the standard deviation σ_{WM} in a white matter region of the brain. Afterwards, these parameters are used in a global Zscore transformation:

$$\text{WhiteStripe}(I) = \frac{I - \mu_{\text{WM}}}{\sigma_{\text{WM}}} \quad (6)$$

This results in an image where the local intensity value distribution of the white matter ROI has zero mean and unit standard deviation. In a similar fashion other normalization types besides Zscore can be adapted. For instance, for a deep learning based MRI liver tumor segmentation⁵⁰, a Minmax normalization was applied by linearly mapping the 2% and 98% percentiles $I_{2\%}^{\text{Liver}}$ and $I_{98\%}^{\text{Liver}}$ of the local intensity distribution within a ROI in the liver, to 0 and 1. In detail, the following transformation was applied voxel-wise:

$$\text{LiverROI-Norm}(I) = \frac{I - I_{2\%}^{\text{Liver}}}{I_{98\%}^{\text{Liver}} - I_{2\%}^{\text{Liver}}} \quad (7)$$

2.3 Reference Metrics

Reference metrics are based on comparing a reference image R with another image I . Both images are assumed to have the same spatial dimensions, i.e. $I, R \in \mathbb{R}^w \times \mathbb{R}^h (\times \mathbb{R}^d)$. An overview on the reference metrics analyzed in this study is given in Tab. 2. If the image I was not acquired with the same modality or the same time point as image R , spatial alignment has to be ensured before applying a reference metric. Typically, this is achieved by image registration techniques.

For natural images, a large set of reference metrics has been benchmarked on the Tampere Image Dataset²⁹ or the LIVE Image Quality Assessment Database³¹. Many of the standard metrics from natural imaging have been frequently applied to medical images. However, some careful modifications are necessary for images with a data type other than 8-bit unsigned integer. In the following, we explain each reference metric in detail and highlight important adaptations.

2.4 Structural Similarity Index Measure

The structural similarity index measure (SSIM) combines local image structure s , luminance l and contrast c . Mean, standard deviation and covariance are calculated locally for each pixel location \mathbf{x} , commonly within a d -dimensional Gaussian kernel of size 11 and $\sigma = 1.5$ and are denoted by $\mu_I(\mathbf{x})$, $\sigma_I(\mathbf{x})$, $\mu_R(\mathbf{x})$, $\sigma_R(\mathbf{x})$ and $\sigma_{I,R}(\mathbf{x})$ respectively. For each pixel location \mathbf{x} , the SSIM is defined locally as:

$$\text{local-SSIM}(I, R, \mathbf{x}) = \underbrace{\left(\frac{\sigma_{I,R}(\mathbf{x}) + C_3}{\sigma_I(\mathbf{x})\sigma_R(\mathbf{x}) + C_3} \right)^\alpha}_{\text{structure}} \cdot \underbrace{\left(\frac{2\mu_I(\mathbf{x})\mu_R(\mathbf{x}) + C_1}{\mu_I(\mathbf{x})^2 + \mu_R(\mathbf{x})^2 + C_1} \right)^\beta}_{\text{luminance}} \cdot \underbrace{\left(\frac{2\sigma_I(\mathbf{x})\sigma_R(\mathbf{x}) + C_2}{\sigma_I(\mathbf{x})^2 + \sigma_R(\mathbf{x})^2 + C_2} \right)^\gamma}_{\text{contrast}} \quad (8)$$

where C_1, C_2, C_3 are constants to avoid division by arbitrarily small numbers. The local-SSIM is then averaged for all pixel locations \mathbf{x} . Commonly, structure, luminance and contrast terms are weighted equally with $\alpha = \beta = \gamma$. Choosing in addition $C_3 = C_2/2$ yields a simplified formula:

$$\text{SSIM}(I, R) = \frac{1}{|I|} \sum_{\mathbf{x} \in R} \frac{(2\mu_I(\mathbf{x})\mu_R(\mathbf{x}) + C_1) \cdot (2\sigma_{I,R}(\mathbf{x}) + C_2)}{(\mu_I(\mathbf{x})^2 + \mu_R(\mathbf{x})^2 + C_1) + (\sigma_I(\mathbf{x})^2 + \sigma_R(\mathbf{x})^2 + C_2)} \quad (9)$$

Table 2. Overview of reference and non-reference metrics. The dark highlighted methods are analyzed in the experiments section.

	abbr	description	low \rightarrow high sim.	implementation	ref.
SSIM	SSIM	structural similarity index measure: combination of structure, luminance and contrast	0 \nearrow 1	torchmetrics ⁵¹ , scikit-image ⁵²	53
	MS-SSIM	Multi-Scale SSIM: SSIM on original and 4 downscaled image resolutions	0 \nearrow 1	torchmetrics ⁵¹	54
	CW-SSIM	Complex Wavelet SSIM ignores phase shifts in the wavelet domain, ignore small rotations and spatial translations	0 \nearrow 1	gitHub ⁵⁵	26
PSNR	PSNR	peak signal-to-noise-ratio: relation of data range to MSE	0 \nearrow ∞	torchmetrics ⁵¹ , scikit-image ⁵²	56
Error Metrics	NMSE	normalized mean squared error	$\infty \searrow$ 0		
	MSE	mean squared error	$\infty \searrow$ 0	scikit-learn ⁵⁷	
	MAE	mean absolute error	$\infty \searrow$ 0	scikit-learn ⁵⁷	
Learned Metrics	LPIPS	Learned perceptual image patch similarity	0 \nearrow 1	pypi ⁵⁸ , torchmetrics ⁵¹	59
	DISTS	Deep Image Structure and Texture Similarity Metric	0 \nearrow 1	gitHub ^{55,60}	28
Statistical Dependence	MI	mutual information: correlation of bin contents	0 \nearrow ∞	itk ⁶¹	62
	NMI	normalized mutual information: MI with fixed range	1 \nearrow 2	scikit-image ⁵²	
	PCC	Pearson Correlation Coefficient	0 \nearrow 1	scikit-learn ⁵⁷	
Indirect	DICE	segmentation metric on downstream segmentation task	0 \nearrow 1	itk ⁶¹	
Non-Reference Metrics	BLUR	Blurriness by difference to additionally blurred image version		scikit-image ⁵²	23
	BLUR2	Blurriness by edge detection and detection of blurred pixels		-	63
	MLC	Mean Line Correlation (also average structural noise): mean correlation between neighbored rows and columns		-	64
	MSLC	Mean Shifted Line Correlation (also average nyquist ghosting): mean correlation between rows and columns, that are with half image distance apart		-	64

The other constants are commonly selected as $C_1 = (0.01 \cdot L)^2$ and $C_2 = (0.03 \cdot L)^2$ with $L = 255$ defined as the data range of the intensity values, in the common case of 8-bit unsigned integers, $L = 255$ ⁵³. The upper bound for the SSIM is 1 and it is achieved when two identical images are given as input. The SSIM decreases with lower similarity down to 0, which constitutes its lower bound.

Several variants of SSIM exist. Multi-scale SSIM (MS-SSIM)⁵⁴ is more sensitive towards differences in downsampled versions of the images to be compared. This puts less impact on high resolution details, which can be undesired for synthesis of high resolution images. The complex-wavelet SSIM (CW-SSIM)²⁶ was specifically designed to compensate for small rotations and spatial translations. As a drawback of ignoring phase shifts in the wavelet domain, artificial phase shifts could be introduced, when CW-SSIM is used for model optimization⁶⁵.

SSIM was developed for natural images with an 8-bit unsigned integer format and the data range parameter L is then set to 255. For non-normalized MR images with a 16-bit range, $L = 2^{16}$ could be used, however the non-quantitative MR acquisition should rather be normalized to a floating point value range before metric assessment. The correct choice of parameter L or parameters C_1 , C_2 and C_3 in case of floating point data is still being discussed. While data dependent choices of the constants are proposed as well as prior normalization by quantiles⁶⁶, current implementations assume a fixed range of $[-1, 1]$ and thereby set $L = 2$ for all floating point valued images⁵² or suggest to use the actual value range $L = [I_{\min}, I_{\max}]$ as data range⁵¹. When the data range parameter L is chosen very high, the three components of SSIM are dominated by the constants C_1 , C_2 and C_3 and SSIM approaches 1, and thereby is less informative. The lower the data range parameter L is chosen for the same input images I and R , the more the SSIM value decreases. Smaller SSIM values induced by a smaller L , may underestimate similarity. The choice for the data range L parameter is directly related to the aforementioned image normalization techniques that rescale the image intensities. For example, if images I and R are rescaled from an assumed value range of $B = b_{\max} - b_{\min}$ to a target range $[0, 1]$, then calculating SSIM with $L = 1$ on these rescaled images will be the same as calculating SSIM on the unscaled images with $L = B$.

We propose to set $L = \max(I_{\max}, R_{\max}) - \min(I_{\min}, R_{\min})$ to ensure symmetry $SSIM(I, R) = SSIM(R, I)$. If image normalization methods are used, the data range parameter L should be adjusted to according to the minimum and maximum values of the normalized images R' and I' .

2.5 Peak signal-to-noise ratio

Peak signal-to-noise ratio (PSNR) was developed to measure the reconstruction quality of a lossy compressed image compared to the uncompressed reference image⁵⁶. However, it is frequently used as a metric for assessing image similarity. The PSNR is infinite for identical images and decreases monotonically as the differences between image I and reference R increase. The peak signal L is analogous to the data range parameter in SSIM and is then divided by the noise, which is measured as the mean square error (MSE, see 2.6).

$$PSNR(I, R) = 10 \cdot \log_{10} \left(\frac{L^2}{MSE(I, R)} \right) = 20 \cdot \log_{10}(L) - \log_{10}(MSE(I, R)) \quad (10)$$

As in SSIM (see Sec. 2.4), the data range L has to be chosen with care based on the actual value range of the data and the utilized normalization techniques. Eq. (10) indicates that the PSNR is minimal, i. e. 0, when $L = \sqrt{MSE(I, R)}$, and for $L > \sqrt{MSE(I, R)}$, PSNR strictly increases with increasing parameter L . For natural images, improved variants of PSNR called PSNR-HVS and PSNR-HVS-M, that seem to correlate closer to the human visual system²⁹, have been developed.

2.6 Error Metrics

This group of metrics, including mean absolute error (MAE), mean square error (MSE), root mean square error (RMSE) and normalized mean square error (NMSE), directly depends on the difference $R(\mathbf{x}) - I(\mathbf{x})$ at each pixel location \mathbf{x} . σ_R denotes the corrected sample standard deviation of image R intensity value distribution.

$$\begin{aligned} MAE(I, R) &= \frac{1}{|I|} \sum_{\mathbf{x}} |R(\mathbf{x}) - I(\mathbf{x})| & MSE(I, R) &= \frac{1}{|I|} \sum_{\mathbf{x}} (R(\mathbf{x}) - I(\mathbf{x}))^2 \\ RMSE(I, R) &= \sqrt{\frac{1}{|I|} \sum_{\mathbf{x}} (R(\mathbf{x}) - I(\mathbf{x}))^2} & NMSE(I, R) &= \frac{1}{|I| \cdot \sigma_R} \sum_{\mathbf{x}} (R(\mathbf{x}) - I(\mathbf{x}))^2 \end{aligned} \quad (11)$$

Due to the convex shape of the quadratic function, the metrics MSE, RMSE, and NMSE give more weight to large differences than MAE. By normalization with σ_R , NMSE assigns a higher similarity to images with a higher standard deviation, i. e. with high variation and a large range of intensity values. On the contrary, the same sum of differences leads to a lower similarity, if the reference image has a very low standard deviation, i. e. it appears very homogeneous. However, the scale of all these metrics strongly depends on the intensity value ranges and thereby also on the normalization method.

2.7 Learned Metrics: LPIPS and DISTs

Learned perceptual image patch similarity (LPIPS) relies on image feature maps from a trained image classification model. In detail, for measuring the similarity between images I and R , the LPIPS metric extracts feature maps $F_l^i(I)$ and $F_l^i(R)$ from layer l and channel i of the pre-trained network. The feature maps are unit-scaled to $\hat{F}_l^i(I), \hat{F}_l^i(R)$, weighted channel-wise with vectors w_l and subtracted. Then the corresponding L_2 norms are averaged spatially and summed to obtain the LPIPS distance $LPIPS(I, R)$:

$$LPIPS(I, R) = \sum_l \frac{1}{|F_l|} \sum_{\mathbf{x}_l} |w_l \odot (\hat{F}_l^i(I) - \hat{F}_l^i(R))(\mathbf{x}_l)|_2^2 \quad (12)$$

where \mathbf{x}_l denotes a pixel location in feature map F_l , \odot denotes the channel-wise multiplication and $|\cdot|_2$ denotes the euclidean norm. For the LPIPS metric, an Alex-Net or VGG-architecture trained for classification on ImageNet was employed and the linear weights w_l^i were optimized by jointly training a second network to predict human judgements on a dataset comprising these judgement for distorted image patch pairs named Berkeley-Adobe Perceptual Patch Similarity (BAPPS) Dataset⁵⁹. The VGG version of LPIPS was recommended for usage as a loss, while the Alex-Net version is preferred as a forward metric and is faster. We analyzed LPIPS with Alex-Net in Sec. 3. Even though the networks were trained on RGB images, the input images are rescaled from $[0, 255]$ to $[-1, 1]$ by Minmax normalization for training. Therefore, images with other intensity value ranges should be similarly rescaled. LPIPS has shown great correlation with human perception and outperforms many other similarity metrics on natural images⁵⁹. It has occasionally been used for validation of medical image synthesis⁶⁷, and is commonly applied as perceptual loss for training medical image-to-image translation models³⁴.

The Deep Image Structure and Texture Similarity (DISTs) metric is an adaption of LPIPS giving more focus on texture. For measuring the similarity between images I and R , the DISTs metric relies again on feature maps $F_l^i(I)$ and $F_l^i(R)$ from layer l and channel i of a pre-trained network. The structure similarity S_l^i and the texture similarity T_l^i between the feature maps were defined as

$$S_l^i(I, R) = \frac{2 \mu_{F_l^i(I)} \cdot \mu_{F_l^i(R)} + C_1}{\mu_{F_l^i(I)}^2 + \mu_{F_l^i(R)}^2 + C_1} \quad T_l^i(I, R) = \frac{2 \sigma_{F_l^i(I)} \cdot \sigma_{F_l^i(R)} + C_2}{\sigma_{F_l^i(I)}^2 + \sigma_{F_l^i(R)}^2 + C_2} \quad (13)$$

where C_1 and C_2 are positive constants. The overall DISTs metric is obtained by averaging weighted combinations of structure and texture similarities across network layers at different depths levels

$$DISTs(I, R) = \sqrt{\sum_l \sum_i (\alpha_l^i S_l^i(I, R) + \beta_l^i T_l^i(I, R))^2} \quad (14)$$

where α_l^i, β_l^i are weighting factors for each channel i and layer l . Compared to LPIPS, the max-pooling layers in the feature extraction network were replaced by ℓ_2 -pooling layers for better anti-aliasing⁶⁸, and the input image was added as a zeroth feature map on top of the convolved and downsampled feature maps from the feature extraction network. The euclidean feature distance measurement is replaced by global SSIM feature distance measurement and weighting factors α_l^i, β_l^i were optimized to achieve similar scores on different samples of equal textures from a texture dataset²⁸.

2.8 Statistical Dependency Metrics: MI, NMI and PCC

Mutual information (MI) and normalized mutual information (NMI) estimate the amount of information of an image R , that can be predicted from image I . MI is widely used as an optimization criterion for multi-modal image registration⁶². It has been used sporadically as a metric for validation of image synthesis^{35,46}.

Given an input and a reference image, both images are transformed to an integer value range $B = [0, b - 1]$, where b is the number of bins, i.e. the number of (equally sized) sub-ranges, that are each mapped to a value in B . This is called equidistant binning or digitization. The binning transformation of an image M is given by:

$$\text{Bin}(M) = \min(b - 1, \lfloor \text{Minmax}_{M_{\min} \rightarrow 0, M_{\max} \rightarrow b}(M) \rfloor) \quad (15)$$

Let I and R denote the binned input and reference images. The joint probability distribution $p(I = i, R = r)$ represents the likelihood of pairs of intensity values $i = I(\mathbf{x})$ and $r = R(\mathbf{x})$ occurring at any pixel location \mathbf{x} in I and R . The joint probability distribution is computed by counting how many pixel locations \mathbf{x} in I and R and dividing this number by the number of pixels $|I|$. Given an intensity $i \in [0, b - 1]$, the probability $p(I = i)$ is computed as the number of pixel locations \mathbf{x} with $I(\mathbf{x}) = i$ divided by the total number of pixels:

$$p(I = i) = \frac{|\{\mathbf{x} \mid I(\mathbf{x}) = i\}|}{|I|} \quad p(R = r) = \frac{|\{\mathbf{x} \mid R(\mathbf{x}) = r\}|}{|R|} \quad (16)$$

The Mutual information MI is then defined as

$$\text{MI}(I, R) = \sum_{i,r} p(I=i, R=r) \log \left(\frac{p(I=i, R=r)}{p(I=i)p(R=r)} \right) \quad (17)$$

where the sum is taken over all possible intensity values $i, r \in [0, b-1]$ in the images I and R . MI can be expressed in terms of the entropy $H(I)$, $H(R)$ and $H(I, R)$ related the distributions $p(I)$, $p(R)$ and $p(I, R)$, respectively. We have:

$$\begin{aligned} H(I) &= -\sum_i p(I=i) \log p(I=i) & H(R) &= -\sum_r p(R=r) \log p(R=r) \\ H(I, R) &= -\sum_{i,r} p(I=i, R=r) \log p(I=i, R=r) & \text{MI}(I, R) &= H(I) + H(R) - H(I, R) \end{aligned} \quad (18)$$

From this, we can derive that bounds for the value range of MI are given by $0 \leq \text{MI}(I, R) \leq \min(H(I), H(R)) \leq \log(|I|)$. A high value of MI indicates that there is a significant amount of shared information between the two images, implying strong dependency or similarity. The upper bound is attained for $I = R$. The normalized variant NMI is an adaptation of the MI metric that accounts for the variations in the entropy of the images being compared. NMI is particularly useful in scenarios where images have different entropy levels, as it normalizes the MI value to provide a more standardized measure of similarity. NMI adjusts the raw MI by considering the joint entropy of the images. It is defined as follows:

$$\text{NMI}(I, R) = \frac{\text{MI}(I, R)}{H(I, R)} + 1 = \frac{H(I) + H(R)}{H(I, R)} \quad (19)$$

The NMI has a fixed value range of $[1, 2]$, which is preferable for comparing absolute metric scores and interpretability. A maximum similarity is achieved for $I = R$, resulting in a maximum NMI value of 2.

The Pearson correlation coefficient (PCC), is a statistical dependency metric which measures the degree of linear dependency between the intensities in I and R at each pixel location. For images I and R the PCC is defined as:

$$\text{PCC}(I, R) = \frac{\sum_{\mathbf{x}} (I(\mathbf{x}) - \mu_I)(R(\mathbf{x}) - \mu_R)}{\sqrt{\sum_{\mathbf{x}} (I(\mathbf{x}) - \mu_I)^2} \sqrt{\sum_{\mathbf{x}} (R(\mathbf{x}) - \mu_R)^2}} \quad (20)$$

where the summations are taken over all pixel locations \mathbf{x} and $R(\mathbf{x})$, $I(\mathbf{x})$ denote the respective intensity values at that location. The value range of the PCC is $[0, 1]$. In case of perfect linear correlation between I and R the upper PCC value bound of 1 is obtained. The PCC may indicate very low similarity if the relation between pixel values in image I and R is non-linear. The lower bound 0 is obtained if the intensity distributions of I and R are uncorrelated. As PCC is defined by correlation and NMI and MI both operate on normalized binned images, previous normalization that purely scales and shifts, such as Minmax, Zscore or Quantile normalization, do not have any effect on the resulting scores.

2.9 Indirect Evaluation with Downstream Tasks

Medical image-to-image translation is most often performed in order to improve medical diagnosis or treatment. In this context, synthetic images must be interpreted in the same way as the reference image, but deviations, that are meaningless for interpretation can be accepted.

As an example, if a synthetic MR image is generated for detecting a brain tumor, it is irrelevant if healthy brain tissue in the synthetic image is brighter or slightly differently structured than in the true reference image, as long as it is clearly identified as healthy tissue. If a synthetic histology image is rated with the same grade of cancer as the reference image, the exact cell-wise correspondence might not be important. Many downstream tasks can be performed automatically and can include segmentation, classification, data augmentation, multi-modal registration or radiation therapy planning (see Tab. 3). Detection, Segmentation and classification metrics for the biomedical domain have been well documented and discussed^{40,41}.

Therefore, the performance of such tasks with synthetic images can be well compared to the performance with reference images to validate the use of synthetic images for a specific task. The concept of downstream task evaluation metrics recognizes that the final goal of image synthesis in the medical domain is to generate useful and correct images rather than images, that are visually appealing. However, if image synthesis was optimized regarding a certain downstream task, the resulting images might not be optimal for other non-related tasks. Specifically, they might have a fake appearance, that does not interfere with the downstream task, but would be misleading for direct review of medical practitioners. Furthermore, the evaluation of downstream tasks can substantially depend on the performance of the downstream task method. If a segmentation model fails on a large set of the reference images, the comparison to segmentations on the synthetic images is obsolete.

The amount and variety of downstream tasks and corresponding metrics is almost unlimited, but to discuss and analyze the value of downstream tasks, we include the evaluation of a downstream segmentation model with a popular segmentation metric,

Table 3. Overview on selected downstream task types, examples and task specific metrics.

Task	Example	Task Metrics
Detection or segmentation of organs, cells and lesions	Segmentation of brain tumors from T1-weighted native, contrast enhanced, T2-weighted and fluid attenuation inversion recovery (FLAIR) MR images ⁴²	DICE, Intersection over Union (IoU)
Classification of images or image segments	Synthesis of clinical skin images with 26 types of conditions, verified by classification scores of dermatologists ⁶⁹	Accuracy, Precision, Recall, F1-Score
Transfer learning and data augmentation	Synthesis of chest X-ray for data augmentation and evaluation of classification model with and without synthetic training data on real data by accuracy, sensitivity, specificity, and area under the receiver-operator-characteristic curve (AUROC) ⁷⁰	Any metric on the test set of the trained task
Multi-modal registration	registration of synthesized MR image from CT image to MRI atlas instead of registration of CT image to MRI atlas ⁷¹	MSE, MI
Dose calculation in radiation therapy planning	Synthesis of a planning CT from MRI for use in a radiation planning tool ⁷²	relative difference of planned radiation dose

namely the DICE score^{40,73}. For segmentations S_I and S_R of images I and R respectively, the DICE score relates the intersection of both segmentations to the sum of their sizes.

$$\text{DICE}(S_I, S_R) = \frac{2|S_I \cap S_R| + \varepsilon}{|S_I| + |S_R| + \varepsilon} \quad (21)$$

The small constant $\varepsilon > 0$ is typically introduced, to assure that the DICE is not undefined in case both segmentations are empty. The upper bound of 1 for the DICE score is attained if the segmentation maps S_I, S_R coincide. For $\varepsilon = 0$ the lower bound is attained when the segmentations do not overlap, i.e. $S_I \cap S_R = \emptyset$. For $\varepsilon > 0$ the lower bound is attained if $S_I = S_R$.

2.10 Non-Reference Quality Metrics

Non-reference metrics, often also called quality metrics or blind metrics, try to assess the quality of a distorted image without knowing the undistorted reference. As a reference might not be available, these metrics can be applied in many evaluation settings. However, there is a huge amount of such metrics and most of them assume a certain kind of distortion to be detected. The correlation of many of these metrics with human perception has been investigated²⁵. Blurriness metrics were quite successful in detecting images with reduced quality as perceived by humans in different image domains.

In this paper, we select and present only a very small set of quality metrics (see Tab. 2), that could possibly complement reference metrics and detect especially those distortions, that are missed by (some) reference metrics. It has often been discussed^{74,75}, that error metrics are not sensitive to blurring, and that synthesis models typically struggle with blurry results. That is why we specifically present blurriness metrics, that do not need a reference. In addition, we would like to assess metrics, that detect MR typical distortions, such as ghosting or stripe artifacts⁶⁴.

2.10.1 Blurriness Metrics: BLUR and BLUR2

Several metrics have been investigated to measure the sharpness or, inversely, the blurriness of images to filter out low-quality images²⁵.

The BLUR²³ metric estimates the strength of blur in an image I without requiring a reference image. For each dimension $d = 1, \dots, n$ of I , a blurred version \tilde{I} of image I is created by convolution with a uniform kernel $U_{k,d}$ of size k along d . The absolute differences of neighboring pixels along d are in \tilde{I} and I as \tilde{D}_d and D_d respectively. D_d and \tilde{D}_d can be seen as the gradients or edge images of the original image I and its blurred version \tilde{I} . Then the sum of positive differences $D - \tilde{D}$ is related to the sum of differences D only as a measure of blurriness. BLUR is implemented in the scikit-image python library⁵² with a default of $k = 11$. In detail, we compute for all d :

$$\begin{aligned} \tilde{I}_d &= \text{conv}(U_{k,d}, I) \\ D_d &= |\nabla_d(I)| & S_d &= \sum_{\mathbf{x}} D_d(\mathbf{x}) \\ \tilde{D}_d &= |\nabla_d(\tilde{I}_d)| & \tilde{S}_d &= \sum_{\mathbf{x}} \max(0, D_d(\mathbf{x}) - \tilde{D}_d(\mathbf{x})) \end{aligned} \quad (22)$$

where $\nabla_d(I)$ denotes the differential of image I in dimension d and \mathbf{x} denotes all pixel locations in D_d . The final BLUR metric is defined as

$$\text{BLUR} = \max_d \frac{S_d - \tilde{S}_d}{S_d} \quad (23)$$

Notably, we have $0 \leq S_d - \tilde{S}_d \leq S_d$ and hence BLUR has a value range of $[0, 1]$. For strongly blurred images we have $\tilde{D}_d \approx D_d$ implying $\tilde{S}_d \approx 0$ and $\text{BLUR} \approx 1$. For sharp images, the uniform smoothing has a large impact on high frequency image features leading to a decreased edge intensity \tilde{D}_d in the blurred image compared to D_d computed on the original image I and hence \tilde{S}_d substantially subtracts from S_d to obtain a low BLUR metric value. Furthermore, we remark that the kernel size has a direct impact on the metric value. The BLUR metric can be easily generalized to images of higher dimensions. The BLUR2 metric⁶³ relies in principal on the ratio of blurred pixels B and non-blurred edge pixels E . In order to identify edge pixels, the image gradient along dimension d and the mean absolute value μ_{D_d} are computed:

$$D_d = |\nabla_d(I)| \quad \mu_{D_d} = \frac{1}{|I|} \sum_{\mathbf{x}} D_d(\mathbf{x}) \quad (24)$$

With two further criteria, a binary map of edge pixels $E_d(\mathbf{x}) \in \{0, 1\}$ is derived from D_d . First, all pixels with gradient values lower or equal to the mean gradient are set to 0 in the edge candidate gradient map C_d . Second, the gradient value must exceed the values of its direct neighbors in dimension d :

$$C_d(\mathbf{x}) = \begin{cases} D_d(\mathbf{x}) & , \text{ if } D_d(\mathbf{x}) > \mu_{D_d} \\ 0 & , \text{ otherwise} \end{cases} \quad E_d(\mathbf{x}) = \begin{cases} 1 & , \text{ if } C_d(\mathbf{x}) > C_d(\mathbf{x}_1, \dots, \mathbf{x}_d + 1, \dots, \mathbf{x}_n) \\ & \text{ and } C_d(\mathbf{x}) > C_d(\mathbf{x}_1, \dots, \mathbf{x}_d - 1, \dots, \mathbf{x}_n) \\ 0 & , \text{ otherwise} \end{cases} \quad (25)$$

In order to determine blurred pixels, the inverse blurriness R_d for dimension d is defined. The inverse blurriness relates the image intensity $I(\mathbf{x})$ to the gradient $D_d(\mathbf{x})$. If the ratios do not exceed a given threshold t_{BR} for any dimension d , the pixel is considered as blurred, in detail:

$$R_d(\mathbf{x}) = \frac{|2I(\mathbf{x}) - D_d(\mathbf{x})|}{D_d(\mathbf{x})} \quad B(\mathbf{x}) = \begin{cases} 1 & , \text{ if } \max_d(R_d(\mathbf{x})) < t_{\text{BR}} \\ 0 & , \text{ otherwise} \end{cases} \quad (26)$$

Based on experiments, the original paper proposes a threshold of $t_{\text{BR}} = 0.1$. The final BLUR2 metric is defined as the ratio of the total number of blurred pixels and the total number of edge pixels:

$$\text{BLUR2} = \frac{\sum_{\mathbf{x}} B(\mathbf{x})}{\sum_{\mathbf{x}} \max_d(E_d(\mathbf{x}))} \quad (27)$$

In summary, this metric defines the inverse blurriness measure to determine if a pixel is blurred and two criteria to decide if a pixel lies on an edge. The BLUR2 ratio increases with the number of detected blurred pixels and decreases with the number of detected edge pixels. Typically, in blurry images there is only a small number of edges and in very sharp images, many edges can be detected.

2.10.2 MR Quality Metrics

In MR images, specific artifacts may appear, which are related to image acquisition and reconstruction. These artifacts may not only appear on real images, but could be reproduced in synthetic images, which is undesirable. Therefore, the use of MR specific quality metrics could efficiently improve validation of MR synthesis models.

In order to select the preferred image from a repeated set of image acquisitions of the same patient, Schuppert et al.⁶⁴, evaluated a set of image quality metrics. Mean line correlation (MLC, in⁶⁴ denoted as "average structural noise") and mean shifted line correlation (MSLC, in⁶⁴ denoted as "average nyquist ghosting") were revealed to be among the best metrics to predict which image was preferred among repeated acquisitions. Possibly, these metrics are able to detect common MR acquisition artifacts, such as ghosting or motion artifacts, that would lead to repeated acquisitions. The MLC metric is defined as the mean correlation between neighboring lines of pixels in an image. For an image $I \in \mathbb{R}^{w \times h}$ with h rows and w columns, let $I_c(x)$ denote the x th column and $I_r(y)$ denote the y th row. Then, MLC is defined by the PCC (see Sec.2.8):

$$\text{MLC} = \frac{1}{w} \sum_{x=1}^w \text{PCC}(I_c(x), I_c(x+1)) + \frac{1}{h} \sum_{y=1}^h \text{PCC}(I_r(y), I_r(y+1)) \quad (28)$$

The MSLC metric is defined as the mean correlation between image lines, that are separated by $\lfloor w/2 \rfloor$ or $\lfloor h/2 \rfloor$ respectively.

$$\text{MLC} = \frac{1}{\lfloor w/2 \rfloor} \sum_{x=1}^{\lfloor w/2 \rfloor} \text{PCC}(I_c(x), I_c(x+1)) + \frac{1}{\lfloor h/2 \rfloor} \sum_{y=1}^{\lfloor h/2 \rfloor} \text{PCC}(I_r(y), I_r(y+1)) \quad (29)$$

These metrics are easily generalizable to images of higher dimension.

3 Experiments

In order to systematically investigate reference and non-reference metrics, we distorted 100 MR images with 11 different types of distortions in five strengths. For the reference metrics (see Sec. 2.3), the similarity between each distorted image and its undistorted reference was calculated. For the non-reference metrics (see Sec. 2.10), the metric scores for all distorted and undistorted images were assessed. For the segmentation metric (see Sec. 2.9), we trained a model and predicted segmentations for all distorted and undistorted images. The segmentation metric assessed the agreement between segmentations derived from distorted images and segmentations derived from the respective undistorted reference image. In addition, images were left with raw intensity values or individually normalized with one of four different normalization methods.

In image-to-image tasks, MR input or target images are typically normalized for model training and the synthesized images are generated in this normalized space. Validation of synthesized images can either be performed in this normalized space, such that the normalized target image is used as reference and the synthesized image is assumed to already be normalized appropriately. Another possibility is to invert the previously performed normalization method on the synthesized image to the original intensity range. Then the synthesized image can be compared to the target image in the original intensity range. In our experiments, we test the metrics in the original and a normalized intensity range. As some distortions slightly or more drastically extend or reduce the intensity range of the reference image, different normalization methods result in different alignment of histograms of the reference and the distorted images. Examples of differently normalized reference and distorted images and their histograms are shown in the appendix Figs. A.1 and A.2.

The LPIPS metric requires an input range of $[-1, 1]$ and the DISTS metric requires an input range of $[0, 1]$. When conducting experiments with different normalization methods, we decided to apply MinMax or cMinMax normalization to the required target range of $[-1, 1]$ for LPIPS and $[0, 1]$ for DISTS respectively. As raw inputs are not recommended, we did not investigate LPIPS or DISTS with raw input images. However, we evaluated with Zscore and Quantile normalization, which don't strictly normalize to $[-1, 1]$ but to a similar range around 0. For DISTS, we additionally added 1 and divided by 2 after Zscore or Quantile normalization, in order to ensure a range near $[0, 1]$. In the following, details of the data, the segmentation model and the distortions are described in detail.

3.1 Data

The data was taken from the BraSyn 2023 challenge⁷⁶ training set, which consists of 1251 T1-weighted (T1n), T1-weighted contrast-enhanced (T1c), T2-weighted (T2w), T2-weighted FLAIR (T2f) and tumor segmentation masks of three classes (whole tumor, tumor core, enhancing tumor). We selected the first 100 cases of the T1c training set images as reference images. For better visualization and reduced computation time, we extracted the centered 2D slice of each 3D volume.

3.2 Segmentation model for downstream task

We trained an automatically configuring U-Net based segmentation network⁷⁷ on the T1c images of the BraSyn dataset to perform a segmentation task with three classes (1: whole tumor, 2: tumor core, 3: enhancing tumor).

The architecture of the U-Net included five residual blocks, with downsampling factors 1, 2, 2, 4 and 4, initially 32 features and one output channel activated by a sigmoid function per class. Although the segmentation masks of the BraSyn data originally consist of 4 classes (3 tumor classes and background), the model was trained with 3 output channels, assuming that a class was present, when the respective output channel exceeded a threshold of 0.5, and when all higher indexed classes were not preset. As a preprocessing step for training and inference, Zscore normalization was applied to the input images. Therefore, no other normalization methods were tested. The segmentations were evaluated with the DICE score (see Eq. 21) for the foreground (class ≥ 1) and for each class individually.

3.3 Distortions

We selected a wide range of distortions, which we expect to appear with MR image synthesis. The parameters of all distortions were scaled to five increasing strengths, where a strength of one should be a minimal distortion, which is not immediately visible and five a strongly visible distortion, which clearly impedes any diagnosis. We initially scaled the distortion parameters to comparable strengths by a reader study with six experienced researchers. The final parameters for each distortion and distorted example images are listed in Tabs. 4 and 5.

Among the selected distortions, translation and elastic deformation were applied as spatial transforms, that are commonly found, when the reference is not well aligned to the image to be tested. This is frequently the case in image-to-image translation, when the input image was acquired with a different modality or at a different time point. Usually, the patient has moved in between and registration was possibly not sufficient. Translation was modeled as an equal shift of all pixels along the x and y-axis and parameterized with a fraction of the image width and height. Elastic deformation was modeled by placing a grid with a given number of points on the image, randomly displacing grid points, and linearly interpolating between the new point positions. The displacements were sampled from a normal distribution with increasing parameter σ and the number of points was reduced for higher distortion strengths.

Intensity distortions, that shift, stretch or compress the histogram, such as gamma transforms or an intensity shift, can appear between different scanning parameters, because MR does not guarantee a fixed intensity scale. For gamma transforms, images are first normalized by Minmax to range $[0, 1]$. This ensures, that the intensity value range is unchanged under gamma transformation, which is simply potentiating with a parameter γ . Then, the intensities are scaled back to the original intensity range. We call gamma transforms for $\gamma > 1$ denominated "Gamma High", while those with $\gamma < 1$ are named "Gamma Low". Both types of distortions are parameterized with increasing or decreasing values of γ respectively for increasing distortion strengths. Intensity shifts are modeled by adding a fraction of the maximum intensity range to the intensity value of all pixels.

Further distortions, that represent typical acquisition artifacts of MR images are ghosting, stripe and bias field artifacts. Ghosting artifacts appear as shifted copies of the image, arising from erroneous sampling in the frequency space. Scaling a single pixel with an intensity parameter in the frequency space causes artificial stripes. Bias fields appear as low frequency background signals, that we model by multiplying with an exponential of a polynomial function of degree three (see Fig. 2). All of these MR acquisition distortions may moderately expand the intensity range of the distorted image compared to the reference image.

Gaussian noise or Gaussian blurring are not restricted to MR acquisition but, as in most imaging modalities, they are frequently observed and were also analyzed in our study. Gaussian noise adds intensity values randomly sampled from a normal distribution with $\mu = 0$ and increasing σ to each pixel intensity. Gaussian blur convolves the reference image with a Gaussian filter with increasing σ .

Last, we investigate the effect of replace artifacts, where parts of the image content are replaced, in this case by mirrored regions. In the BraSyn data set, in most cases, there is a tumor in exactly one hemisphere of the brain. By mirroring one hemisphere onto the other one, a second tumor is inserted into, or a tumor is removed from the second hemisphere. We scaled this distortion by mirroring an increasing fraction of the hemisphere. Replacing brain structures in one hemisphere by structure in the other one, simulates the generation of synthetic structures, that were not in the input image. This is a known problem of some synthesis models, e. g. of cycleGAN architectures⁷⁸. The detection of such synthetically inserted structures is highly desired for image-to-image translation model validation.

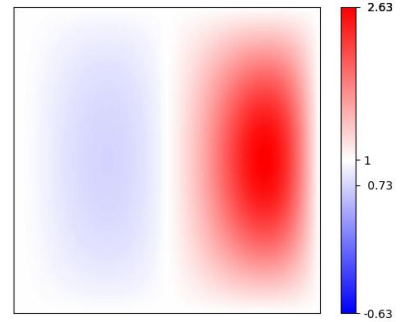
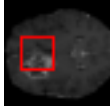
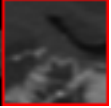


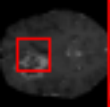

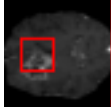

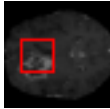
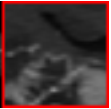
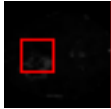

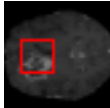
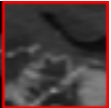
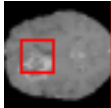
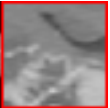
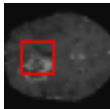
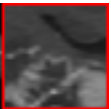
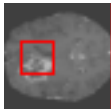


Figure 2. Images were multiplied with a simulated bias field $e^{c \cdot P_3}$ based on the exponential of a polynomial function of order 3:
$$P_3(x_1, x_2) = 10x_1^2(x_1 - 1) \cdot (x_2 - 0.5)x_2(x_2 - 1).$$

Table 4. Distortions based on spatial and intensity transforms. Parameters are given for strengths $s = 1$ and $s = 5$. All other strengths are interpolated linearly between the given values. Calculation of distorted image \tilde{I} . Let $\mathbf{s} = (w, h)$ be the image size vector of I . The minimum and maximum intensity of I are denoted by I_{\min}, I_{\max} .

Distortion		parameter $s = 1 \rightarrow s = 5$	calculation	example images			
				$s = 1$	$s = 5$		
Spatial	Translation	fraction f $0.01 \rightarrow 0.2$	$\tilde{I}(x_1, x_2) = I(f \cdot w + x_1, f \cdot h + x_2)$				
	Elastic Deform	points n $18 \rightarrow 11$ displ. d $0.03 \rightarrow 0.1$	Create a grid with n^2 points, displace points by $\mathcal{N}(\mu = 0; \sigma = d \cdot \frac{s}{n})$				
Intensity	Gamma High	$\log(\gamma)$ $0.095 \rightarrow 0.916$	$\tilde{I} = \text{MinMax}^{-1}(\text{MinMax}(I)^\gamma)$				
	Gamma Low	$\log(\gamma)$ $-0.01 \rightarrow (-0.916)$					
	Shift Intensity	fraction f $0.05 \rightarrow 0.25$		$\tilde{I} = I + f \cdot I_{\max}$			

4 Results

4.1 Reference Metrics

The results for all strengths are given in the appendix in Figs. A.3-A.6. In Tab. 6 - 10, the results for distortions of maximal strength ($s=5$) are summarized.

As all normalization methods cancel the effect of intensity shifting and therefore perfect similarity scores are achieved for all metrics and distortion strengths, the results for intensity shift distortions are not shown in Tabs. 7-10.

For all applied distortions, all reference metric scores monotonously measure lower similarity for increasing distortion strengths. Without applying any normalization, all metrics beside NMI are very sensitive to intensity shifts (see Tab. 6). However, with any normalization method, intensity shifts are fully compensated, and all metrics measure perfect similarity.

Across all normalization methods, all metrics are very sensitive to translation and not very sensitive to replace artifacts.

SSIM similarity scores for strong blurring are very high, compared to most other distortions. Gaussian noise is better detected with Minmax normalization, while stripe artifacts seem to be less detected with Zscore normalization. PSNR scores generally display only very small changes for strengths larger than 2 (see Fig. A.3). PSNR values are higher for Zscore normalization. Images distorted with Gaussian blurring and ghosting artifacts receive very high PSNR similarity scores, especially with small distortion strengths.

All error metrics (MSE, MAE and NMSE) strongly vary in their value range, depending on the normalization method. They are consistently most sensitive to translation and then to bias field, and gamma transforms. With cMinmax normalization, the error metrics are less sensitive to gamma transforms.

The PCC and NMI metrics are invariant to normalizations, that consist of shifting and scaling. Therefore, results for PCC and NMI with Minmax, Zscore or Quantile normalization are omitted. PCC is most sensitive to translation and then to bias field artifacts. Besides gamma high transforms with higher strengths, all other distortions are assigned high similarity with values larger than 0.9 on a $[0, 1]$ range. NMI clearly assigns decreased scores to all distortions, except intensity shift. Especially, translation and ghosting receive low similarity values. Gamma transforms stay almost the same for all strengths > 0 , just decreasing slightly for high strengths of gamma high.

The segmentation scores (see Tab. 6, and Fig. A.6) for all three classes are very similar. The effect of elastic deforms and ghosting artifacts on the segmentation are very limited. Gaussian noise and stripe artifacts most strongly impair segmentation.

Table 5. Other general image distortions and MR acquisition specific artifacts. Parameters are given for strengths $s = 1$ and $s = 5$. All other strengths are interpolated linearly between the given values. Calculation of distorted image \tilde{I} . Let $\mathbf{s} = (w, h)$ be the image size vector of I . The maximum intensity of image I is denoted by I_{\max} . The fast Fourier transform is $\text{FFT}(I)$, $\text{shift}(I)$ moves frequency 0 to the center.

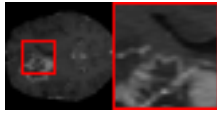
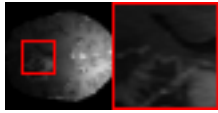
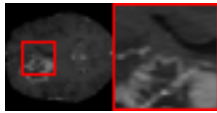
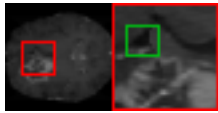
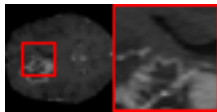
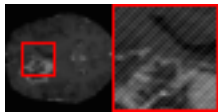
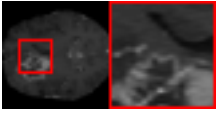
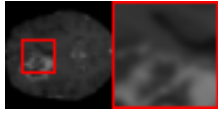
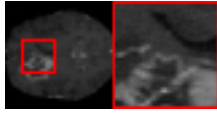
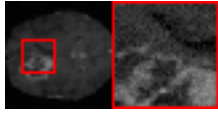
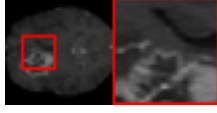
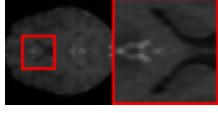
Distortion	parameter $s = 1 \rightarrow s = 5$	calculation	example $s = 1$	images $s = 5$
MR Acquisition Artifacts	Bias Field coefficient c 0.5 \rightarrow 10	$P_3(x_1, x_2) = 10x_1^2(x_1 - 1) \cdot (x_2 - 0.5)x_2(x_2 - 1)$ $\tilde{I} = I \cdot e^{c \cdot P_3}$		
	Ghosting intensity i 0.05 \rightarrow 0.4	$I' = \text{shift}(\text{FFT}(I))$ partially distort spectrum: $I''(x_1, x_2) = I' \cdot i, \text{ for } x_1 \% 2 = 0$ partially restore spectrum: $I''(x_1, x_2) = I', \text{ for } x_1 = w/2$ $\tilde{I} = \text{shift}^{-1}(\text{FFT}^{-1}(I''))$		
	Stripe Artifact intensity i 0.05 \rightarrow 0.5	$I' = \text{FFT}(\text{shift}(I))$ $I''(x_1, x_2) = i \cdot I_{\max}, \text{ for } x_1 = 0.3 \cdot \cos(0), x_2 = 0.3 \cdot \sin(0)$ $\tilde{I} = \text{FFT}^{-1}(\text{shift}^{-1}(I''))$		
Other Distortions	Gaussian Blur σ 0.2 \rightarrow 1.3	$\tilde{I} = \text{Conv}(G_\sigma, I)$ where G_σ is a Gaussian kernel		
	Gaussian Noise σ 0.005 \rightarrow 0.05	$\tilde{I} = I + \mathcal{N}(\mu = 0; \sigma)$		
	Replace Artifact fraction f 0.1 \rightarrow 1.0	$\tilde{I}(x_1, x_2) = \begin{cases} I(x_1, x_2) & , \text{ if } x_2 \leq \frac{h}{2} \\ I(x_1, h - x_2) & , \text{ if } x_2 > \frac{h \cdot (1+f)}{2} \end{cases}$		

Table 6. Similarity of reference images and strongly distorted versions of the same image (strength 5/5) assessed with different metrics, without additional normalization. The darker the background the more sensitive the metric to this distortion. Most metrics are sensitive to translation, except the DISTS metric. Elastic deformation or replace artifacts hardly reduce similarity. Without normalization, most metrics are very sensitive to intensity shifts, except NMI, PCC and DICE, where normalization is included in the metric application.

metric	SSIM	MS-SSIM	CW-SSIM	PSNR	MAE	MSE	NMSE	NMI	PCC	DICE
low→high	0→1	0→1	0→1	0→∞	∞→0	∞→0	∞→0	1→2	0→1	0→1
Distortions										
Bias Field	0.9	0.75	0.75	23.96	591.53	$2.74 \cdot 10^6$	$2.21 \cdot 10^3$	1.28	0.77	0.59
Ghosting	0.88	0.97	0.95	37.44	70.71	$1.81 \cdot 10^4$	14.54	1.37	0.99	0.78
Stripe Artifact	0.27	0.95	0.99	28.14	211.57	$1.25 \cdot 10^5$	100.54	1.36	0.96	0.31
Gaussian Blur	0.94	0.99	1.0	33.94	54.04	$3.92 \cdot 10^4$	31.1	1.41	0.99	0.41
Gaussian Noise	0.39	0.84	0.96	27.92	326.09	$2.02 \cdot 10^5$	163.49	1.16	0.93	0.36
Replace Artifact	0.9	0.87	0.84	27.59	95.73	$1.69 \cdot 10^5$	136.24	1.4	0.94	0.52
Gamma High	0.75	0.55	0.45	18.4	548.52	$1.24 \cdot 10^6$	996.45	1.61	0.8	0.54
Gamma Low	0.89	0.84	0.78	15.38	891.89	$3.35 \cdot 10^6$	$2.66 \cdot 10^3$	1.8	0.98	0.6
Shift Intensity	0.25	0.97	0.86	13.98	$2.27 \cdot 10^3$	$6.68 \cdot 10^6$	$5.33 \cdot 10^3$	2.0	1.0	1.0
Translation	0.65	0.38	0.39	18.28	503.14	$1.19 \cdot 10^6$	963.96	1.07	0.53	0.32
Elastic Deform	0.87	0.92	0.91	28.1	98.88	$1.45 \cdot 10^5$	115.9	1.32	0.95	0.76

Table 7. Similarity of reference images and strongly distorted versions of the same image (strength 5/5) assessed with different metrics, with previous Minmax normalization. The darker the background the more sensitive the metric to this distortion. Most metrics are sensitive to translation, except the DISTS metric. Elastic deformation or replace artifacts hardly reduce similarity. With Minmax normalization, distortions that extend or reduce the intensity range, such as Gaussian Noise and ghosting have a larger effect on the metric.

metric	SSIM	MS-SSIM	CW-SSIM	PSNR	MAE	MSE	NMSE	LPIPS	DISTS
low→high	0→1	0→1	0→1	0→∞	∞→0	∞→0	∞→0	1→0	1→0
Distortions									
Bias Field	0.86	0.69	0.6	20.97	0.05	0.01	0.07	0.17	0.17
Ghosting	0.31	0.96	0.9	21.18	0.09	0.01	0.07	0.07	0.17
Stripe Artifact	0.27	0.95	0.99	28.12	0.03	0.0	0.01	0.3	0.38
Gaussian Blur	0.93	0.96	0.96	25.68	0.03	0.01	0.04	0.19	0.21
Gaussian Noise	0.17	0.83	0.85	15.95	0.16	0.03	0.2	0.65	0.38
Replace Artifact	0.89	0.87	0.84	26.79	0.02	0.0	0.02	0.07	0.1
Gamma High	0.75	0.55	0.45	18.4	0.07	0.02	0.12	0.25	0.3
Gamma Low	0.89	0.84	0.78	15.38	0.09	0.03	0.25	0.1	0.16
Translation	0.65	0.38	0.39	18.28	0.06	0.02	0.12	0.36	0.08
Elastic Deform	0.87	0.92	0.91	27.56	0.01	0.0	0.01	0.06	0.1

Table 8. Similarity of reference images and strongly distorted versions of the same image (strength 5/5) assessed with different metrics, with previous cMinmax_{5%} normalization. The darker the background the more sensitive the metric to this distortion. Most metrics are sensitive to translation, except the DISTS metric. Elastic deformation or replace artifacts hardly reduce similarity. With cMinmax normalization, the effect of distortions that extend or reduce the intensity range, such as Gaussian Noise and ghosting is smaller than for Minmax normalization, but higher than for Zscore or Quantile normalization. Gamma transforms also receive much higher similarity scores compared to other normalization methods.

metric	SSIM	MS-SSIM	CW-SSIM	PSNR	MAE	MSE	NMSE	LPIPS	DISTS	NMI	PCC
low→high	0→1	0→1	0→1	0→∞	∞→0	∞→0	∞→0	1→0	1→0	1→2	0→1
Distortions											
Bias Field	0.83	0.69	0.65	11.95	0.12	0.07	0.17	0.15	0.2	1.26	0.8
Ghosting	0.71	0.96	0.95	27.29	0.03	0.0	0.0	0.05	0.16	1.3	0.99
Stripe Artifact	0.14	0.88	0.97	18.51	0.08	0.01	0.04	0.52	0.4	1.36	0.95
Gaussian Blur	0.91	0.98	0.99	25.99	0.02	0.0	0.01	0.23	0.2	1.36	0.99
Gaussian Noise	0.15	0.69	0.89	14.22	0.16	0.04	0.1	0.81	0.35	1.13	0.93
Replace Artifact	0.86	0.86	0.86	19.38	0.03	0.01	0.03	0.08	0.09	1.38	0.96
Gamma High	0.93	0.93	0.89	19.17	0.05	0.01	0.03	0.07	0.13	1.84	0.97
Gamma Low	0.94	0.94	0.92	22.81	0.03	0.01	0.02	0.07	0.11	1.82	0.99
Translation	0.59	0.32	0.4	8.83	0.18	0.13	0.34	0.41	0.08	1.07	0.56
Elastic Deform	0.81	0.9	0.91	20.0	0.03	0.01	0.03	0.08	0.11	1.29	0.97

Table 9. Similarity of reference images and strongly distorted versions of the same image (strength 5/5) assessed with different metrics, with previous Zscore normalization. The darker the background the more sensitive the metric to this distortion. Most metrics are sensitive to translation, except the DISTS metric. Elastic deformation or replace artifacts hardly reduce similarity. With Zscore normalization, the effect of distortions that extend or reduce the intensity range, such as Gaussian Noise and ghosting is reduced. Gamma transforms also receive higher similarity scores compared to other normalization methods.

metric	SSIM	MS-SSIM	CW-SSIM	PSNR	MAE	MSE	NMSE	LPIPS	DISTS
low→high	0→1	0→1	0→1	0→∞	∞→0	∞→0	∞→0	1→0	1→0
Distortions									
Bias Field	0.8	0.72	0.71	24.62	0.42	0.46	0.46	0.15	0.26
Ghosting	0.97	0.97	0.96	37.85	0.08	0.01	0.01	0.09	0.19
Stripe Artifact	0.54	0.95	1.0	28.85	0.23	0.09	0.09	0.53	0.35
Gaussian Blur	0.94	0.99	1.0	33.98	0.07	0.03	0.03	0.25	0.19
Gaussian Noise	0.45	0.84	0.97	28.03	0.3	0.14	0.14	0.82	0.32
Replace Artifact	0.89	0.87	0.85	27.73	0.11	0.12	0.12	0.09	0.09
Gamma High	0.85	0.89	0.8	35.05	0.36	0.41	0.41	0.18	0.3
Gamma Low	0.95	0.94	0.89	32.29	0.1	0.04	0.04	0.09	0.17
Translation	0.58	0.37	0.41	18.28	0.49	0.93	0.93	0.44	0.1
Elastic Deform	0.87	0.92	0.92	28.09	0.1	0.11	0.11	0.09	0.1

Table 10. Similarity of reference images and strongly distorted versions of the same image (strength 5/5) assessed with different metrics, with previous Quantile normalization. The darker the background the more sensitive the metric to this distortion. The pattern of sensitive metrics is very similar to the result with Zscore normalization, especially reduced sensitivity to Gamma transforms, ghosting and Gaussian noise.

metric	SSIM	MS-SSIM	CW-SSIM	PSNR	MAE	MSE	NMSE	LPIPS	DISTS
low→high	0→1	0→1	0→1	0→∞	∞→0	∞→0	∞→0	1→0	1→0
Distortions									
Bias Field	0.88	0.67	0.66	22.28	0.82	5.01	7.7	0.15	0.26
Ghosting	0.86	0.97	0.95	37.23	0.05	0.01	0.01	0.09	0.19
Stripe Artifact	0.23	0.95	0.98	26.81	0.21	0.07	0.1	0.53	0.35
Gaussian Blur	0.94	0.98	1.0	33.51	0.04	0.02	0.02	0.25	0.19
Gaussian Noise	0.24	0.84	0.95	26.66	0.24	0.1	0.14	0.82	0.32
Replace Artifact	0.9	0.87	0.85	27.7	0.07	0.06	0.09	0.09	0.09
Gamma High	0.94	0.81	0.57	33.26	0.41	9.29	9.66	0.18	0.3
Gamma Low	0.95	0.91	0.84	29.49	0.08	0.05	0.06	0.09	0.17
Translation	0.65	0.38	0.39	18.32	0.32	0.41	0.61	0.44	0.1
Elastic Deform	0.87	0.92	0.91	28.05	0.07	0.06	0.08	0.09	0.1

Translated segmentations have decreasing overlap and thereby very low DICE scores. As Zscore normalization is included and recommended for the segmentation model, the DICE scores with other normalization methods are not included in Tabs. 7 - 10.

4.2 Non-Reference Metrics

The results for all strengths are given in Fig. A.7. For the maximum strength (s=5), the results are summarized in Tab. 11 without normalization and for cMinmax normalization.

Minmax, Zscore and Quantile normalization do not have any effect on the selected non-reference metrics, therefore these results are not shown here.

For the BLUR metric, scores clearly increase for blurred images, but also clearly decrease compared to the reference for stripe artifacts, Gaussian noise and the gamma transform for $\gamma > 1$. For small strengths of translation and elastic deformation slightly increased blurriness is measured, but drops again for strengths > 3 .

Compared to the reference images, MSLC strongly drops for images with stripe artifacts. With cMinmax normalization, MSLC also detects ghosting.

MLC decreased most strongly for stripe artifacts, Gaussian noise and ghosting. The difference for higher distortion strengths is only small, while the lowest distortions are already detected.

5 Adverse Examples

In the following, special characteristics of the analyzed metrics, which can be derived from their definition or the experimental results above, are show-cased. We present adverse examples (see Fig. 3-8), where similarity metrics do not perform as intended or expected.

Table 11. Non-reference metric results without normalization (Left) and with cMinmax normalization with clipping at 5% (Right). The darker the background the more sensitive the metric to this distortion.

metric	BLUR	MSLC	MLC	metric	BLUR	MSLC	MLC
$\Delta \rightarrow$ Reference				$\Delta \rightarrow$ Reference			
Bias Field	0.37	0.15	0.97	Bias Field	0.39	0.16	0.97
Ghosting	0.34	0.19	0.84	Ghosting	0.36	0.27	0.85
Stripe Artifact	0.2	0.37	0.32	Stripe Artifact	0.2	0.37	0.32
Gaussian Blur	0.52	0.21	0.99	Gaussian Blur	0.52	0.21	0.99
Gaussian Noise	0.18	0.14	0.52	Gaussian Noise	0.18	0.14	0.53
Replace Artifact	0.33	0.17	0.97	Replace Artifact	0.35	0.17	0.97
Gamma High	0.27	0.12	0.92	Gamma High	0.32	0.15	0.95
Gamma Low	0.35	0.17	0.97	Gamma Low	0.35	0.17	0.98
Shift Intensity	0.33	0.16	0.96	Shift Intensity	0.35	0.17	0.97
Translation	0.33	0.16	0.97	Translation	0.35	0.17	0.97
Elastic Deform	0.36	0.18	0.97	Elastic Deform	0.37	0.19	0.98
Reference	0.33	0.16	0.96	Reference	0.35	0.17	0.97

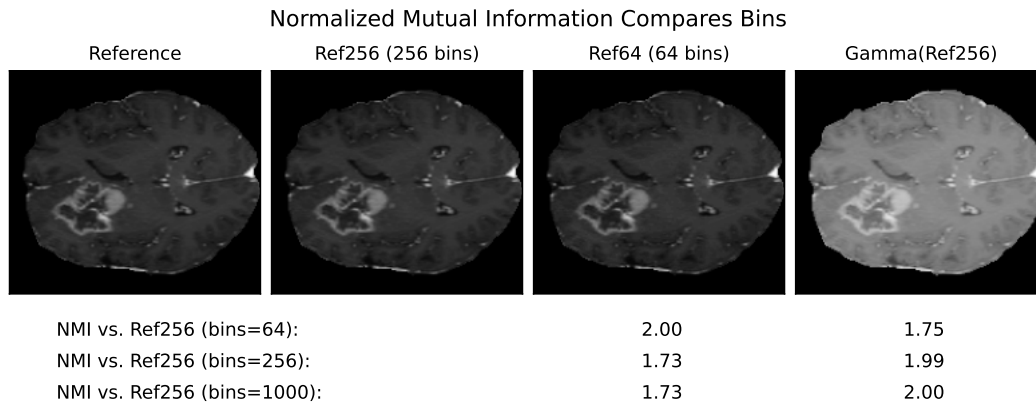


Figure 3. For calculation of NMI, images need to be discretized to histograms. The number and distance of bins chosen to compare an image with its reference has large influence to the resulting NMI score. An image reduced to 6-bit (64 bins) already decreases the NMI score, calculated with 256 bins (8-bit) to 1.73, although the difference is hardly visible. If NMI also uses only 64 bins, a perfect NMI score of 2.0 is obtained. At the same time, a gamma transformed image can achieve a perfect NMI score, if the intensities of one bin in the reference image are mapped into a unique bin in the transformed images as well. With 1000 bins used for NMI calculation, all intensities of one bin in the reference image end up in one and the same separate bin in the gamma transformed image. The strong visual difference in contrast in the gamma transformed image is not captured by NMI.

How much background is in the metric?

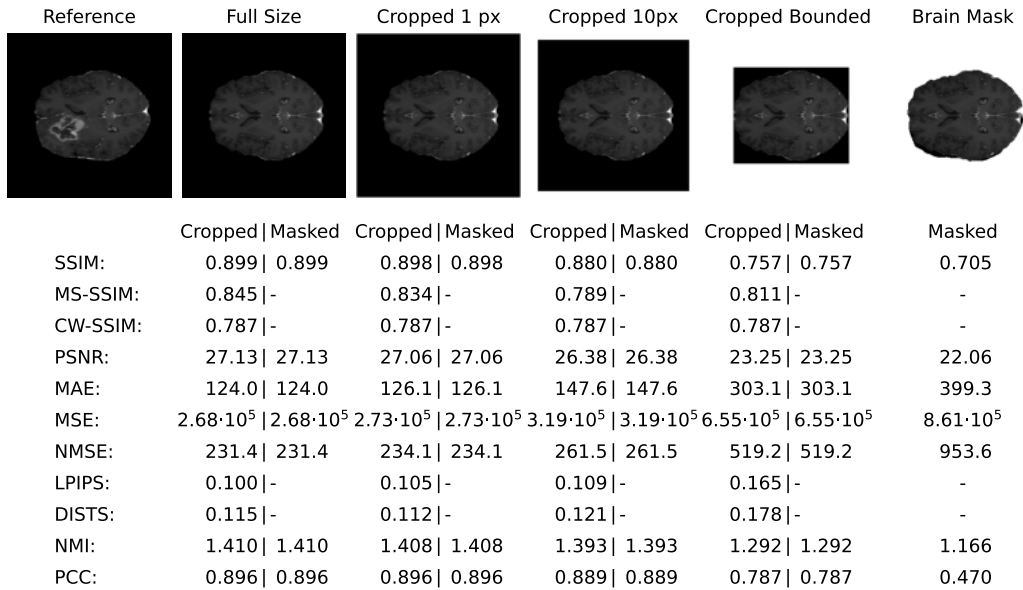


Figure 4. When metric evaluation is not restricted to a foreground region, the size of included background influences the metric score. The reference image is compared to an image, where the lower 50% of the image are replaced by the mirrored upper 50%. The background is reduced by cropping or masking. A region restricted (masked) evaluation, is not clearly defined for all metrics. The current CW-SSIM implementation includes automatic padding to a power of 2. Therefore, all shown crops are padded back to the full size and the CW-SSIM value remains unchanged. All other metrics decrease with less background, which is perfectly equal and therefore contributes to a higher similarity.

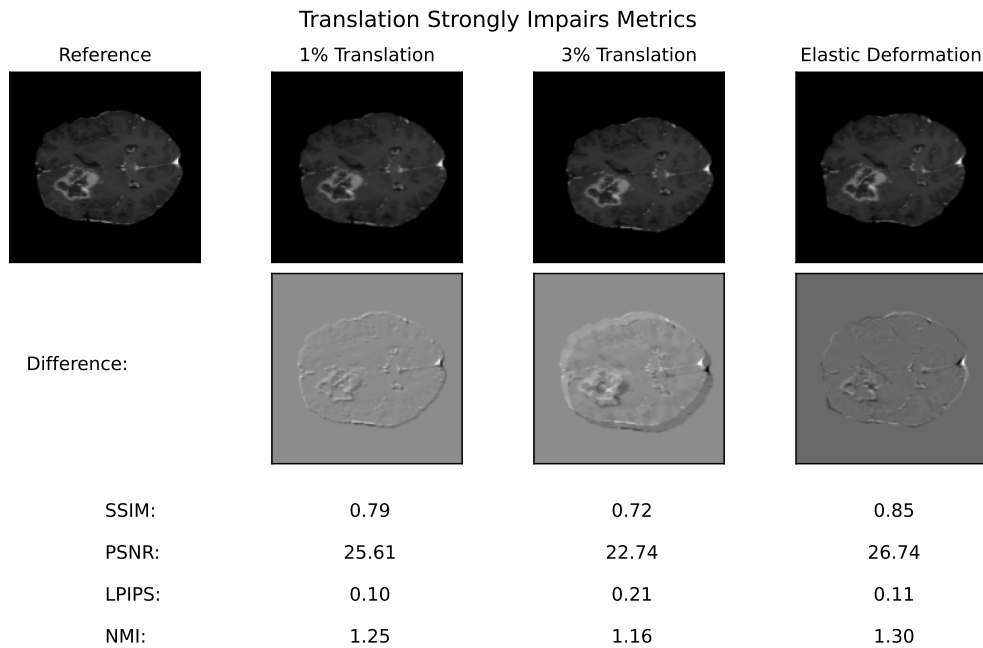


Figure 5. Metric assessed similarity strongly decreases, when images to be compared are only slightly misaligned. For translation of all pixels, the decrease is stronger than for elastic deformation, which effects a smaller set of pixels. Misalignment can be a problem for confirming high similarity between synthesized and target images.

Blurring Improves SSIM of Distorted Images

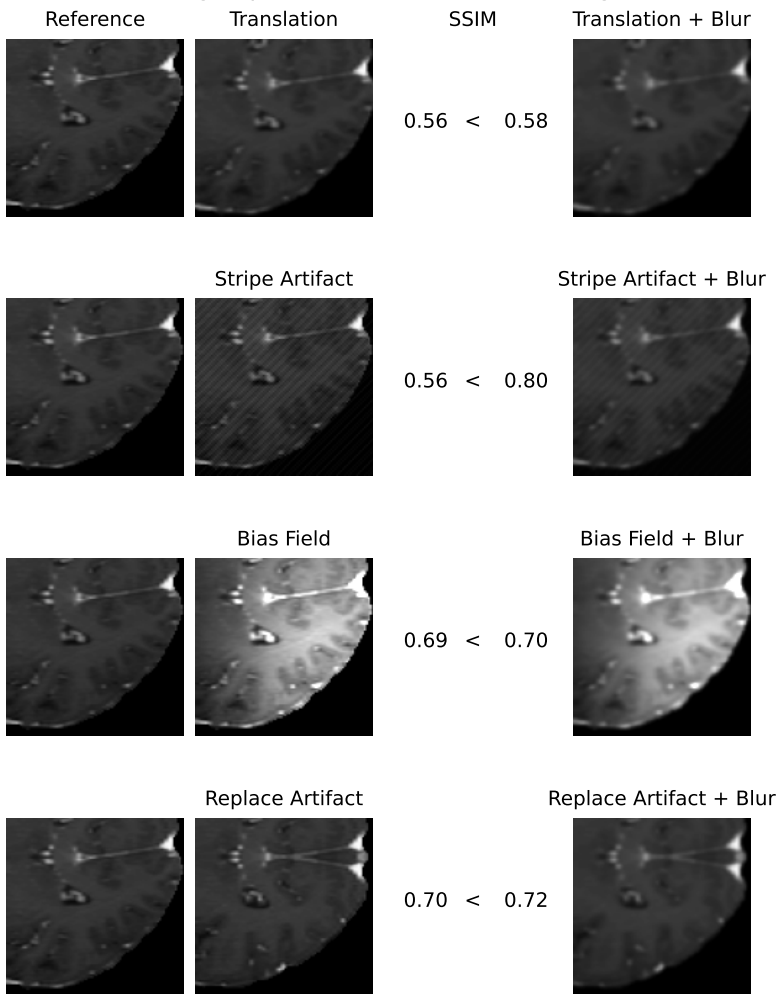


Figure 6. Images distorted by translation, stripe artifacts, bias field or replace artifacts, show larger similarity to the reference, when they are additionally blurred. Partially, this might be expected, because distortions are weakened by blurring. But in image synthesis trained with SSIM, this may lead to blurry results.

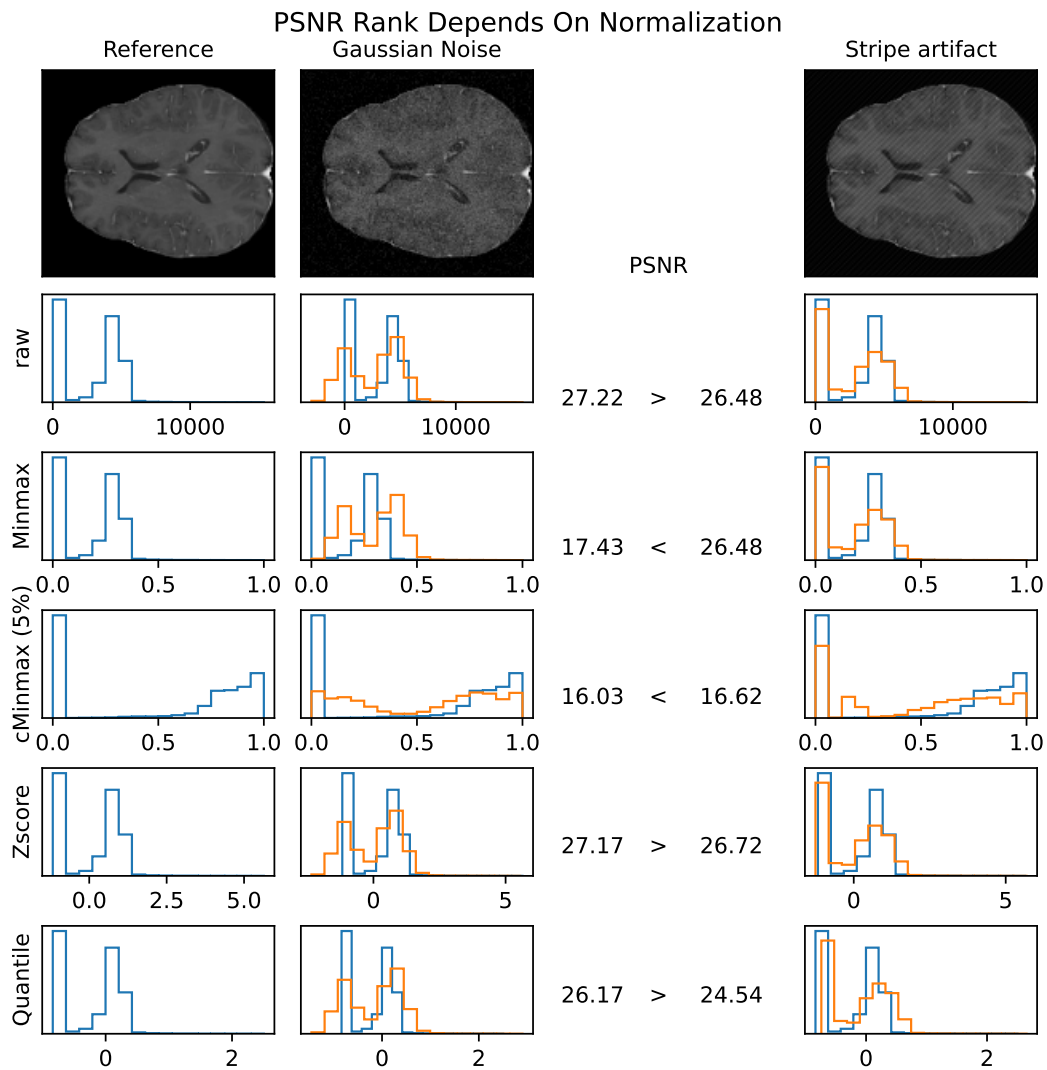


Figure 7. PSNR scores strongly depend on the normalization method. After normalization of images with Gaussian blur or stripe artifacts with different methods very different PSNR values are obtained. When comparing two images to the same reference, the PSNR values may even rank the images differently, depending on the normalization method. Therefore, PSNR values and rankings cannot be compared between studies, when the exact normalization methods is not reported.

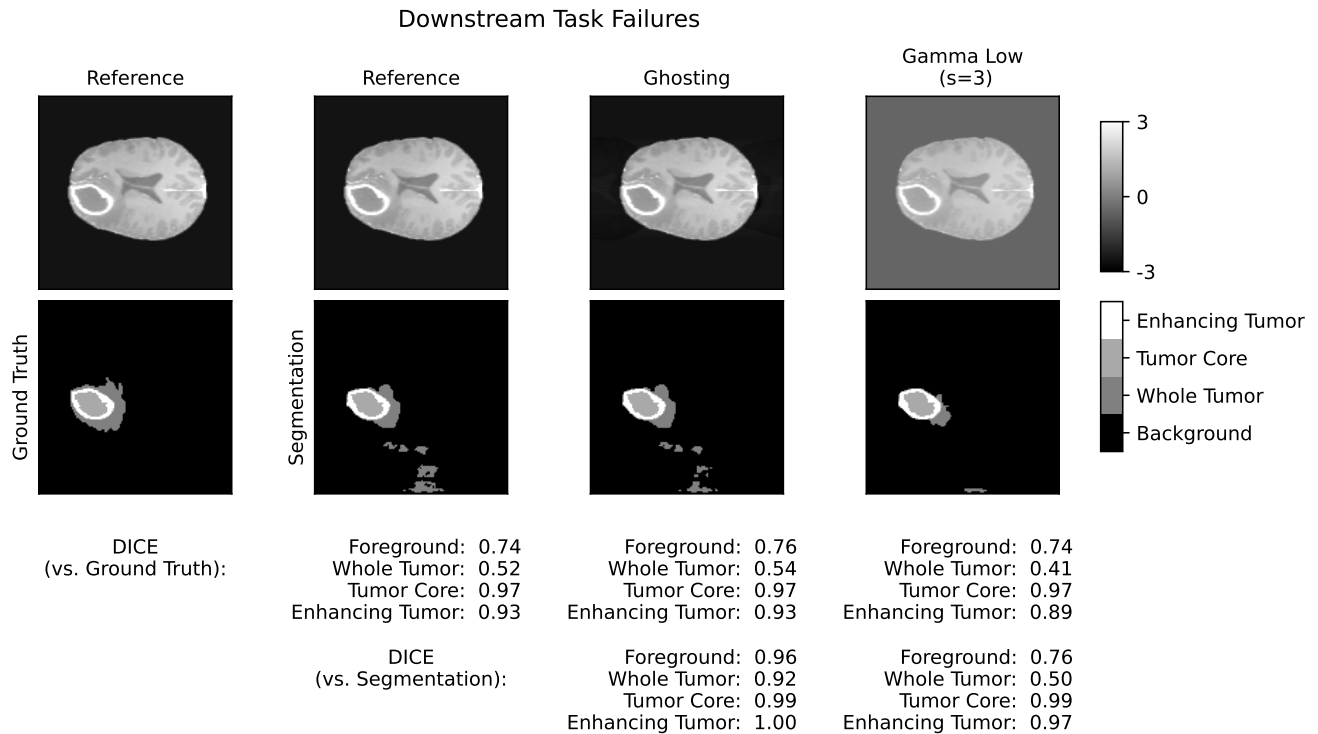


Figure 8. The evaluation with a downstream task is limited to the performance of the downstream task. In this example a large fraction of background is segmented as "whole tumor". The segmentation model was trained on smaller crops with less background and without background artifacts. Although the segmentation of the gamma transformed image seems to better fit the ground truth in the true tumor region, the dice score is noticeably lower, than for the segmentation of the image with ghosting, which displays very similar background artifacts as the reference segmentation. A different segmentation model, or a human could have segmented the tumor nearly equally well as in the reference image by simply ignoring the background. The dice scores between distorted and reference image segmentations do not correlate well with the similarity between distorted and reference image in the tumor region.

6 Discussion

The experiments and adverse examples demonstrate specific strengths and weaknesses of the analyzed metrics. Although SSIM and PSNR are frequently used for the evaluation of synthetic MR images, they are strongly decreased by constant intensity shifts if no normalization is applied. PSNR is very dependent on the kind of normalization, which complicates its use as a comprehensive metric for comparing studies of different authors. SSIM underestimates blurring and thereby favors blurred or additionally blurred images over other distortions.

As most other analyzed metrics, SSIM and PSNR are both very sensitive to translation, which is rather caused by misaligned target images, than by dissimilarity of synthesized images. When paired input and target images are not acquired by the same hardware or not immediately at the same time points, special care must be taken, to ensure spatial alignment of input and target images. CW-SSIM is able to ignore small translations of strength 1. due to construction in the complex-wavelet domain. The DISTS metric, that focuses more on texture, than spatial alignment does not fully ignore translation, but does not increase strictly with the degree of translation. Variations in similarity between translated image versions could be caused by interpolation at non-integer pixel size shifts.

Some of these observations have already been mentioned by other authors. Similar to SSIM, MSE and MAE were reported to create blurry images⁷⁹. And PSNR and MSE were mentioned to be sensitive to the normalization method⁴⁶.

Replace artifacts remain underestimated by most similarity metrics. For those artifacts, that resemble structures of diagnostic interest, the evaluation of segmentations with a specific segmentation model is useful. In our evaluation, we use a segmentation model, that was trained to detect different tumor regions. It successfully detects replace artifacts, where the tumor is doubled or removed.

The non-reference metrics can give valuable additional information about the quality of synthesized images. Blurring is easily and reliably detected by the BLUR metric. However, assessed blurriness decreases with other distortions, such as Gaussian noise, stripe artifacts or gamma transforms, when these increase image contrast. Translation also varies the measured blurriness, which is most likely caused by interpolation.

The MLC metric represents the line-wise correlation between neighboring lines. The reference value in our experiments lies at 96%, which is probably caused by high anatomical consistency in the present pixel spacing. It strongly decreases for stripe artifacts, which fits to the fact, that the stripes change relations between local image intensities and are not oriented along the x- or y-axis. Random Gaussian noise reduces statistical correlation and thereby also MLC. Ghosting also reduces MLC, as it additionally distorts image intensities locally.

The MSLC metric only slightly increases with ghosting. One reason could be the relative weak scaling of the ghost intensity in our experiments. In contrast, stripe artifacts significantly increased the MSLC metrics. Compared to MLC, by coincidence, stripes seem to be in the same phase at the half-image width distance and thereby drastically increase line-wise correlation. Normalization methods are able to partially reverse certain kinds of distortions. Shift intensity is fully removed by any of the tested normalization methods. Gamma transforms are alleviated by cMinmax, because intensity values are compressed at very high and low intensity values. Bias field correction⁸⁰, which was not investigated in this study, was designed to remove bias field artifacts and can be applied as a normalization step.

Our experiments were performed on T1-weighted contrast-enhanced MR images from the BraSyn dataset. Future work should include a much broader set of MR images with other sequences and body regions to make sure, that the results are valid more generally. The background in the BraSyn dataset takes up a large fraction of the image and was specifically preprocessed and set to 0. These factors largely influence some of the metrics, especially SSIM, PSNR and the error based metrics and therefore other data could yield different experimental results. However, we found that using masks with these metrics can efficiently reduce this bias.

In comparison to other metric benchmarks, we do not compare the metric scores to human quality assessment. For each type of distortion, we tried to select five comparable strengths. As shown in Tabs. 4 and 5, the lowest and highest strengths were scaled to appear almost not visible or to decrease quality to an equally poor level. Even though distortion parameters might not be scaled perfectly to human perception, the overall qualitative observations about which metrics are most sensitive towards which kind of distortions and the following conclusions are valid.

7 Conclusions

For the validation of medical image-to-image translation, we gave a broad overview of possible metrics. For 11 reference, three non-reference metrics and a segmentation metric, we presented a detailed study of their sensitivity to 11 types of distortions, which are specific for MR images.

As a conclusion, we give a few recommendations for the selection and application of appropriate validation metrics.

- As reference metrics the combination of SSIM, LPIPS, MSE and NMI is able to detect a large set of undesired distortions. MS-SSIM, PCC, DISTS, NMSE, and MAE do not give much additional information. MSE is the most frequently used

error metric and therefore best suited for comparison to previous studies. The use of PSNR should not be recommended. CW-SSIM only when reference images are known to be slightly misaligned.

- As non-reference quality metrics, BLUR reliably detects blurry images, which might not be detected by SSIM or MSE. MLC can detect artifacts that reduce anatomical consistency and is specifically sensitive to ghosting, stripe artifacts, and Gaussian noise.
- For SSIM, LPIPS and MSE we recommend z-score normalization. NMI should be used without normalization. The normalization method must be reported in detail with all parameters whenever metric scores are reported. Normalization must be considered, when comparing scores across studies. The data range parameter L of SSIM should be set to the actual intensity range and must be reported as part of the normalization method. An appropriate normalization moves similar tissue types to similar intensity values.
- The amount of background should be reduced as far as possible. If methods for masking a metric and appropriate masks for the foreground or region of interest are available, they should be used. The amount of background may also influence the normalization result.
- If input images and target images are not spatially aligned, they must be registered with highest possible precision before evaluating with reference metrics. Rigid translation seems to be more problematic, than small local elastic deformations. CW-SSIM can ignore small translations. The type of interpolation may additionally distort the images.
- A segmentation downstream task is useful for evaluation, because image synthesis models are able to synthesize artificial structures relevant for possible downstream tasks. The segmentation model should therefore be able to segment task specific structures of interest and can be trained with desired or inconsequential distortions. The performance of the segmentation model must be verified before using the segmentations for similarity assessment.

In summary, the metrics for evaluation of image-to-image MR synthesization models must be selected carefully. Frequently used SSIM and PSNR cover a large range of distortions, but have specific weaknesses, that must be covered by other metrics. Specifically PSNR does not seem appropriate for image synthesis evaluation. We highlight some adverse examples, where metrics do not provide the expected or desired values. We suggest further metrics in addition to SSIM, that are able to detect MR specific and typical distortions.

For the selection of metrics and normalization methods, the set of admitted and undesired distortions should be considered. Which metrics are most appropriate to ignore or detect which kind of distortions can be directly derived from our experimental results.

As metrics are also often used as loss functions for model training⁶⁵ or validation metrics for model selection, the choice of appropriate metrics can directly improve image synthesis models before human assessment and speed up model development.

References

1. Saharia, C. *et al.* Palette: Image-to-image diffusion models. In *ACM SIGGRAPH 2022 Conference Proceedings*, SIGGRAPH '22, DOI: [10.1145/3528233.3530757](https://doi.org/10.1145/3528233.3530757) (Association for Computing Machinery, New York, NY, USA, 2022).
2. Isola, P., Zhu, J.-Y., Zhou, T. & Efros, A. A. Image-to-image translation with conditional adversarial networks. In *2017 IEEE Conference on Computer Vision and Pattern Recognition (CVPR)*, 5967–5976, DOI: [10.1109/CVPR.2017.632](https://doi.org/10.1109/CVPR.2017.632) (2017).
3. Goodfellow, I. *et al.* Generative adversarial nets. In Ghahramani, Z., Welling, M., Cortes, C., Lawrence, N. & Weinberger, K. (eds.) *Advances in Neural Information Processing Systems*, vol. 27 (Curran Associates, Inc., 2014).
4. Rezende, D. & Mohamed, S. Variational inference with normalizing flows. In Bach, F. & Blei, D. (eds.) *Proceedings of the 32nd International Conference on Machine Learning*, vol. 37 of *Proceedings of Machine Learning Research*, 1530–1538 (PMLR, Lille, France, 2015).
5. Kingma, D. P. & Welling, M. Auto-encoding variational bayes. In *International Conference on Learning Representations* (2014).
6. Ho, J., Jain, A. & Abbeel, P. Denoising diffusion probabilistic models. In Larochelle, H., Ranzato, M., Hadsell, R., Balcan, M. & Lin, H. (eds.) *Advances in Neural Information Processing Systems*, vol. 33, 6840–6851 (Curran Associates, Inc., 2020).
7. Kebaili, A., Lapuyade-Lahorgue, J. & Ruan, S. Deep Learning Approaches for Data Augmentation in Medical Imaging: A Review. *J. imaging* **9**, DOI: [10.3390/jimaging9040081](https://doi.org/10.3390/jimaging9040081) (2023). Place: Switzerland.

8. Zhu, J.-Y., Park, T., Isola, P. & Efros, A. A. Unpaired image-to-image translation using cycle-consistent adversarial networks. In *2017 IEEE International Conference on Computer Vision (ICCV)*, 2242–2251, DOI: [10.1109/ICCV.2017.244](https://doi.org/10.1109/ICCV.2017.244) (2017).
9. Kaji, S. & Kida, S. Overview of image-to-image translation by use of deep neural networks: denoising, super-resolution, modality conversion, and reconstruction in medical imaging. *Radiol. Phys. Technol.* **12**, 235–248 (2019).
10. Hong, K.-T. *et al.* Lumbar spine computed tomography to magnetic resonance imaging synthesis using generative adversarial network: Visual turing test. *Diagn. (Basel)* (2022).
11. Zhu, L. *et al.* Make-a-volume: Leveraging latent diffusion models for cross-modality 3d brain mri synthesis. In Greenspan, H. *et al.* (eds.) *Medical Image Computing and Computer Assisted Intervention – MICCAI 2023*, 592–601 (Springer Nature Switzerland, Cham, 2023).
12. Ben-Cohen, A., Klang, E., Raskin, S. P., Amitai, M. M. & Greenspan, H. Virtual pet images from ct data using deep convolutional networks: Initial results. In Tsafaris, S. A., Gooya, A., Frangi, A. F. & Prince, J. L. (eds.) *Simulation and Synthesis in Medical Imaging*, 49–57 (Springer International Publishing, Cham, 2017).
13. Li, Q. *et al.* Eliminating ct radiation for clinical pet examination using deep learning. *Eur. J. Radiol.* **154**, 110422 (2022).
14. Ammari, S. *et al.* Can deep learning replace gadolinium in neuro-oncology?: A reader study. *Investig. Radiol.* **57**, 99–107 (2022).
15. Weigert, M. *et al.* Content-aware image restoration: pushing the limits of fluorescence microscopy. *Nat. Methods* **15**, 1090–1097 (2018).
16. Bahrami, A., Karimian, A. & Arabi, H. Comparison of different deep learning architectures for synthetic ct generation from mr images. *Phys. Medica* **90**, 99–107, DOI: <https://doi.org/10.1016/j.ejmp.2021.09.006> (2021).
17. Lu, J., Öfverstedt, J., Lindblad, J. & Sladoje, N. Is image-to-image translation the panacea for multimodal image registration? a comparative study. *PLOS ONE* **17**, 1–33, DOI: [10.1371/journal.pone.0276196](https://doi.org/10.1371/journal.pone.0276196) (2022).
18. Raut, P., Baldini, G., Schöneck, M. & Caldeira, L. Using a generative adversarial network to generate synthetic mri images for multi-class automatic segmentation of brain tumors. *Front. Radiol.* **3**, DOI: [10.3389/fradi.2023.1336902](https://doi.org/10.3389/fradi.2023.1336902) (2024).
19. Mallio, C. A. *et al.* Artificial intelligence to reduce or eliminate the need for gadolinium-based contrast agents in brain and cardiac mri: A literature review. *Investig. Radiol.* **58** (2023).
20. Borji, A. Pros and cons of gan evaluation measures: New developments. *Comput. Vis. Image Underst.* **215**, 103329, DOI: <https://doi.org/10.1016/j.cviu.2021.103329> (2022).
21. Salimans, T. *et al.* Improved techniques for training gans. *CoRR* **abs/1606.03498** (2016). [1606.03498](https://arxiv.org/abs/1606.03498).
22. Heusel, M., Ramsauer, H., Unterthiner, T., Nessler, B. & Hochreiter, S. Gans trained by a two time-scale update rule converge to a local nash equilibrium. In *Proceedings of the 31st International Conference on Neural Information Processing Systems, NIPS'17*, 6629–6640 (Curran Associates Inc., Red Hook, NY, USA, 2017).
23. Crété-Roffet, F., Dolmiere, T., Ladret, P. & Nicolas, M. The Blur Effect: Perception and Estimation with a New No-Reference Perceptual Blur Metric. In *SPIE Electronic Imaging Symposium Conf Human Vision and Electronic Imaging*, vol. XII, EI 6492–16 (San Jose, United States, 2007).
24. Shurcliff, W. A. *Studies in optics: A.a. michelson*, university of chicago press, 1927, republished in 1962 as phoenix science series no. 514 paperback, 176 pp. illustrated, \$1.75. *J. Phys. Chem. Solids* **24**, 498–499 (1963).
25. Pinykh, O. S., Pospelova, K. & Kamboj, N. H. Modeling human perception of image quality. *J. Digit. Imaging* **31**, 768–775 (2018).
26. Sampat, M. P., Wang, Z., Gupta, S., Bovik, A. C. & Markey, M. K. Complex wavelet structural similarity: A new image similarity index. *IEEE Transactions on Image Process.* **18**, 2385–2401, DOI: [10.1109/TIP.2009.2025923](https://doi.org/10.1109/TIP.2009.2025923) (2009).
27. Li, Y. *et al.* Samscore: A semantic structural similarity metric for image translation evaluation (2023). [2305.15367](https://arxiv.org/abs/2305.15367).
28. Ding, K., Ma, K., Wang, S. & Simoncelli, E. P. Image quality assessment: Unifying structure and texture similarity. *IEEE Transactions on Pattern Analysis Mach. Intell.* **44**, 2567–2581, DOI: [10.1109/TPAMI.2020.3045810](https://doi.org/10.1109/TPAMI.2020.3045810) (2022).
29. Ponomarenko, N. *et al.* A new color image database tid2013: Innovations and results. In Blanc-Talon, J., Kasinski, A., Philips, W., Popescu, D. & Scheunders, P. (eds.) *Advanced Concepts for Intelligent Vision Systems*, 402–413 (Springer International Publishing, Cham, 2013).
30. Sheikh, H., Sabir, M. & Bovik, A. A statistical evaluation of recent full reference image quality assessment algorithms. *IEEE Transactions on Image Process.* **15**, 3440–3451, DOI: [10.1109/TIP.2006.881959](https://doi.org/10.1109/TIP.2006.881959) (2006).

31. Live image quality assessment database release 2.
32. Chow, L. S., Rajagopal, H. & Paramesran, R. Correlation between subjective and objective assessment of magnetic resonance (mr) images. *Magn. Reson. Imaging* **34**, 820–831, DOI: <https://doi.org/10.1016/j.mri.2016.03.006> (2016).
33. Nečasová, T., Burgos, N. & Svoboda, D. Validation and evaluation metrics for medical and biomedical image synthesis. In Burgos, N. & Svoboda, D. (eds.) *Biomedical Image Synthesis and Simulation*, The MICCAI Society Book Series, chap. 25, 573–600 (Academic Press, 2022).
34. Yi, X., Walia, E. & Babyn, P. Generative adversarial network in medical imaging: A review. *Med. Image Analysis* **58**, 101552, DOI: <https://doi.org/10.1016/j.media.2019.101552> (2019).
35. McNaughton, J. *et al.* Machine learning for medical image translation: A systematic review. *Bioengineering* **10** (2023).
36. Haase, R. *et al.* Artificial contrast: Deep learning for reducing gadolinium-based contrast agents in neuroradiology. *Investig. Radiol.* **58**, 539–547 (2023).
37. Mudeng, V., Kim, M. & Choe, S.-w. Prospects of structural similarity index for medical image analysis. *Appl. Sci.* **12** (2022).
38. Huynh-Thu, Q. & Ghanbari, M. Scope of validity of psnr in image/video quality assessment. *Electron. Lett.* **44**, 800–801 (2008).
39. <https://www.fda.gov/medical-devices/software-medical-device-samd/artificial-intelligence-and-machine-learning-aiml-enabled-medical-devices>.
40. Reinke *et al.*, A. Understanding metric-related pitfalls in image analysis validation. *Nat. Methods* **21**, 82 – 194 (2024).
41. Maier-Hein *et al.*, L. Metrics reloaded: recommendations for image analysis validation. *Nat. Methods* **21**, 195–212 (2024).
42. Baltruschat, I. M., Janbakhshi, P. & Lenga, M. Brasyn 2023 challenge: Missing mri synthesis and the effect of different learning objectives (2024). [2403.07800](https://arxiv.org/abs/2403.07800).
43. Goodfellow, I., Bengio, Y. & Courville, A. *Deep Learning*, chap. 12.2.1 Preprocessing, 448 (MIT Press, 2016). <http://www.deeplearningbook.org>.
44. Tellez, D. *et al.* Quantifying the effects of data augmentation and stain color normalization in convolutional neural networks for computational pathology. *Med. Image Analysis* **58**, 101544, DOI: <https://doi.org/10.1016/j.media.2019.101544> (2019).
45. Onofrey, J. A. *et al.* Generalizable multi-site training and testing of deep neural networks using image normalization. *Proceedings. IEEE Int. Symp. on Biomed. Imaging* 348–351 (2019).
46. Reinhold, J. C., Dewey, B. E., Carass, A. & Prince, J. L. Evaluating the impact of intensity normalization on MR image synthesis. In Angelini, E. D. & Landman, B. A. (eds.) *Medical Imaging 2019: Image Processing*, vol. 10949, 109493H, DOI: [10.1117/12.2513089](https://doi.org/10.1117/12.2513089). International Society for Optics and Photonics (SPIE, 2019).
47. Haase, R. *et al.* Reduction of gadolinium-based contrast agents in mri using convolutional neural networks and different input protocols: Limited interchangeability of synthesized sequences with original full-dose images despite excellent quantitative performance. *Investig. Radiol.* **58** (2023).
48. Nyúl, L. G. & Udupa, J. K. On standardizing the mr image intensity scale. *Magn. Reson. Medicine* **42**, 1072–1081 (1999).
49. Shinohara, R. T. *et al.* Statistical normalization techniques for magnetic resonance imaging. *NeuroImage: Clin.* **6**, 9–19 (2014).
50. Hänsch, A., Chlebus, G., Meine, H. & *et al.* Improving automatic liver tumor segmentation in late-phase mri using multi-model training and 3d convolutional neural networks. *Sci. Reports* **12**, DOI: <https://doi.org/10.1038/s41598-022-16388-9> (2022).
51. Torchmetrics - measuring reproducibility in pytorch, DOI: [10.21105/joss.04101](https://doi.org/10.21105/joss.04101) (2022).
52. van der Walt, S. *et al.* scikit-image: image processing in Python. *PeerJ* **2**, e453, DOI: [10.7717/peerj.453](https://doi.org/10.7717/peerj.453) (2014).
53. Wang, Z., Bovik, A. C., Sheikh, H. R. & Simoncelli, E. P. Image quality assessment: from error visibility to structural similarity. *IEEE Transactions on Image Process.* **13**, 600–12 (2004).
54. Wang, Z., Simoncelli, E. & Bovik, A. Multiscale structural similarity for image quality assessment. In *The Thirty-Seventh Asilomar Conference on Signals, Systems and Computers, 2003*, vol. 2, 1398–1402 Vol.2, DOI: [10.1109/ACSSC.2003.1292216](https://doi.org/10.1109/ACSSC.2003.1292216) (2003).
55. Ding, K. "iqa optimization" (2020).

56. Huynh-Thu, Q. & Ghanbari, M. Scope of validity of psnr in image/video quality assessment. *Electron. Lett.* **44**, 800–801(1) (2008).
57. Pedregosa, F. *et al.* Scikit-learn: Machine learning in Python. *J. Mach. Learn. Res.* **12**, 2825–2830 (2011).
58. "perceptual similarity metric and dataset".
59. Zhang, R., Isola, P., Efros, A. A., Shechtman, E. & Wang, O. The unreasonable effectiveness of deep features as a perceptual metric. *CoRR* **abs/1801.03924** (2018). [1801.03924](https://arxiv.org/abs/1801.03924).
60. Ding, K.
61. McCormick, M., Liu, X., Ibanez, L., Jomier, J. & Marion, C. Itk: enabling reproducible research and open science. *Front. Neuroinformatics* **8**, DOI: [10.3389/fninf.2014.00013](https://doi.org/10.3389/fninf.2014.00013) (2014).
62. Maes, F., Collignon, A., Vandermeulen, D., Marchal, G. & Suetens, P. Multimodality image registration by maximization of mutual information. *IEEE Transactions on Med. Imaging* **16**, 187–198, DOI: [10.1109/42.563664](https://doi.org/10.1109/42.563664) (1997).
63. Choi, M. G., Jung, J. H. & Jeon, J. W. No-reference image quality assessment using blur and noise. *Int. J. Electr. Comput. Eng.* **3**, 184–188 (2009).
64. Schuppert *et al.*, C. Whole-body magnetic resonance imaging in the large population-based german national cohort study: Predictive capability of automated image quality assessment for protocol repetitions. *Investig. Radiol.* **57** (2022).
65. Ding, K., Ma, K., Wang, S. & Simoncelli, E. P. Comparison of image quality models for optimization of image processing systems. *CoRR* **abs/2005.01338** (2020).
66. Baker, A. H., Pinard, A. & Hammerling, D. M. On a structural similarity index approach for floating-point data. *IEEE Transactions on Vis. Comput. Graph.* 1–13, DOI: [10.1109/TVCG.2023.3332843](https://doi.org/10.1109/TVCG.2023.3332843) (2023).
67. Liu, J. *et al.* One model to synthesize them all: Multi-contrast multi-scale transformer for missing data imputation. *IEEE Transactions on Med. Imaging* **42**, 2577–2591, DOI: [10.1109/TMI.2023.3261707](https://doi.org/10.1109/TMI.2023.3261707) (2023).
68. Hénaff, O. J. & Simoncelli, E. P. Geodesics of learned representations. *Proc. Int. Conf. Learn. Represent.* 1–10 (2016).
69. Ghorbani, A., Natarajan, V., Coz, D. & Liu, Y. DermGAN: Synthetic Generation of Clinical Skin Images with Pathology. In Dalca, A. V. *et al.* (eds.) *Proceedings of the Machine Learning for Health NeurIPS Workshop*, vol. 116 of *Proceedings of Machine Learning Research*, 155–170 (PMLR, 2020).
70. Jang, M. *et al.* Image turing test and its applications on synthetic chest radiographs by using the progressive growing generative adversarial network. *Sci. Reports* **13** (2023).
71. McNaughton, J. *et al.* Synthetic mri generation from ct scans for stroke patients. *BioMedInformatics* **3**, 791–816, DOI: [10.3390/biomedinformatics3030050](https://doi.org/10.3390/biomedinformatics3030050) (2023).
72. Zimmermann, L. *et al.* An mri sequence independent convolutional neural network for synthetic head ct generation in proton therapy. *Zeitschrift fuer Medizinische Physik* **32**, 218–227 (2022).
73. Dice, L. R. Measures of the amount of ecologic association between species. *Ecology* **26**, 297–302, DOI: <https://doi.org/10.2307/1932409> (1945).
74. Jayachandran Preetha, C. *et al.* Deep-learning-based synthesis of post-contrast t1-weighted mri for tumour response assessment in neuro-oncology: a multicentre, retrospective cohort study. *The Lancet Digit. Heal.* **3**, e784–e794, DOI: [https://doi.org/10.1016/S2589-7500\(21\)00205-3](https://doi.org/10.1016/S2589-7500(21)00205-3) (2021).
75. Müller-Franzes, G. *et al.* A multimodal comparison of latent denoising diffusion probabilistic models and generative adversarial networks for medical image synthesis. *Sci. Reports* **13**, 12098 (2023).
76. Li, H. B. & *et al.* The brain tumor segmentation (brats) challenge 2023: Brain mr image synthesis for tumor segmentation brasyn. *arxiv* (2023).
77. Consortium, M. Monai: Medical open network for ai (2023). <https://docs.monai.io/en/stable/auto3dseg.html>.
78. Cohen, J. P., Luck, M. & Honari, S. Distribution matching losses can hallucinate features in medical image translation. In Frangi, A. F., Schnabel, J. A., Davatzikos, C., Alberola-López, C. & Fichtinger, G. (eds.) *Medical Image Computing and Computer Assisted Intervention – MICCAI 2018*, 529–536 (Springer International Publishing, Cham, 2018).
79. Liu, J. *et al.* Dyefreenet: Deep virtual contrast ct synthesis. In Burgos, N., Svoboda, D., Wolterink, J. M. & Zhao, C. (eds.) *Simulation and Synthesis in Medical Imaging*, 80–89 (Springer International Publishing, Cham, 2020).
80. Tustison, N. J. *et al.* N4itk: improved n3 bias correction. *IEEE transactions on medical imaging* **29**, 1310–20 (2010).

Appendix

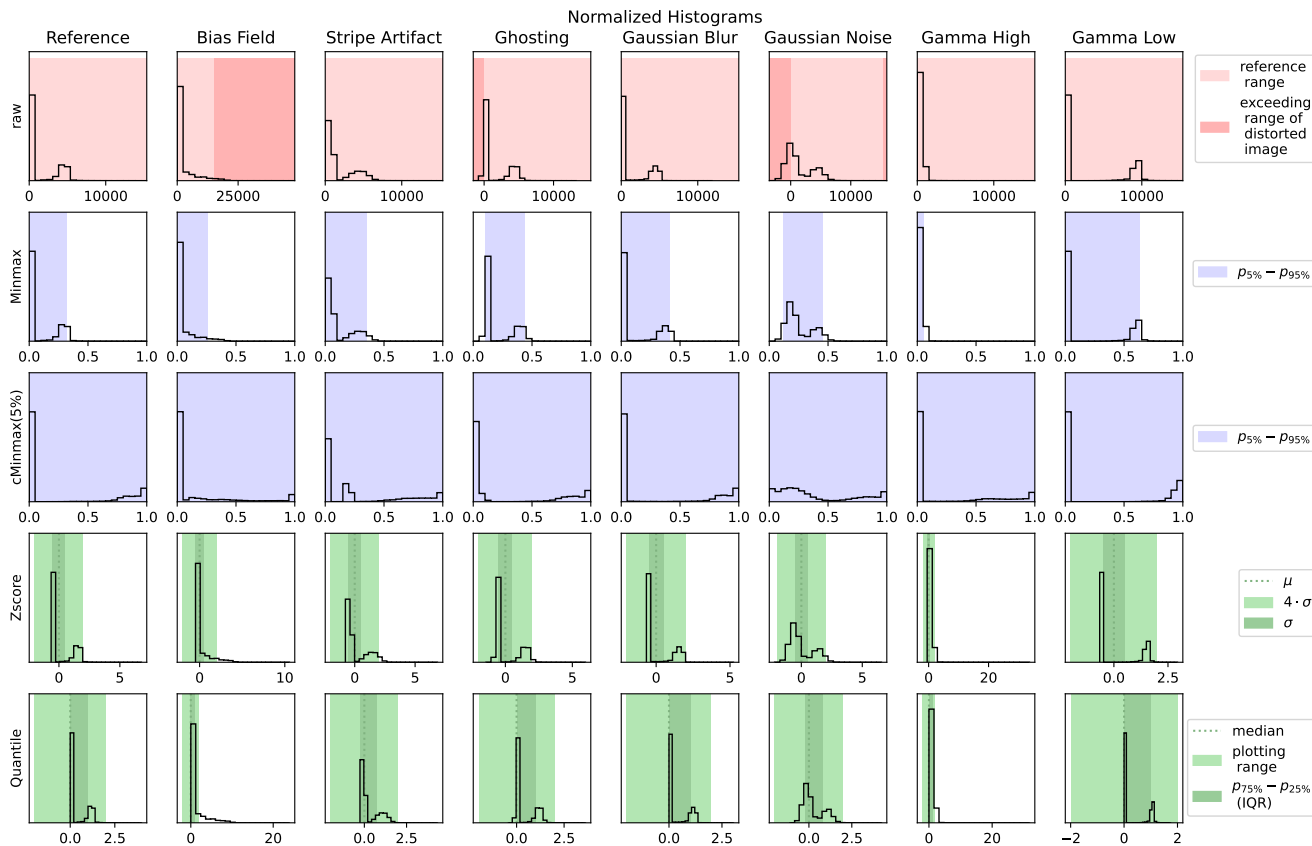


Figure A.1. Normalized histograms of reference distorted images. In the first row, unnormalized raw reference image (first column) and different distortions applied with highest strength (5/5). The shape, position and/or the intensity value range of the histogram changes with the selected distortions. Exceeding value ranges are highlighted with a darker compared to the lighter pink shade of the reference image value range. Minmax normalization scales the x-axis to a [0,1] range, while cMinmax significantly changes the histogram shape by clipping outliers and stretching the rest of the histogram. Zscore and Quantile normalization are similar, but in these images, the mean is higher than the median, and the interquartile range (IQR) is smaller, than the standard deviation.

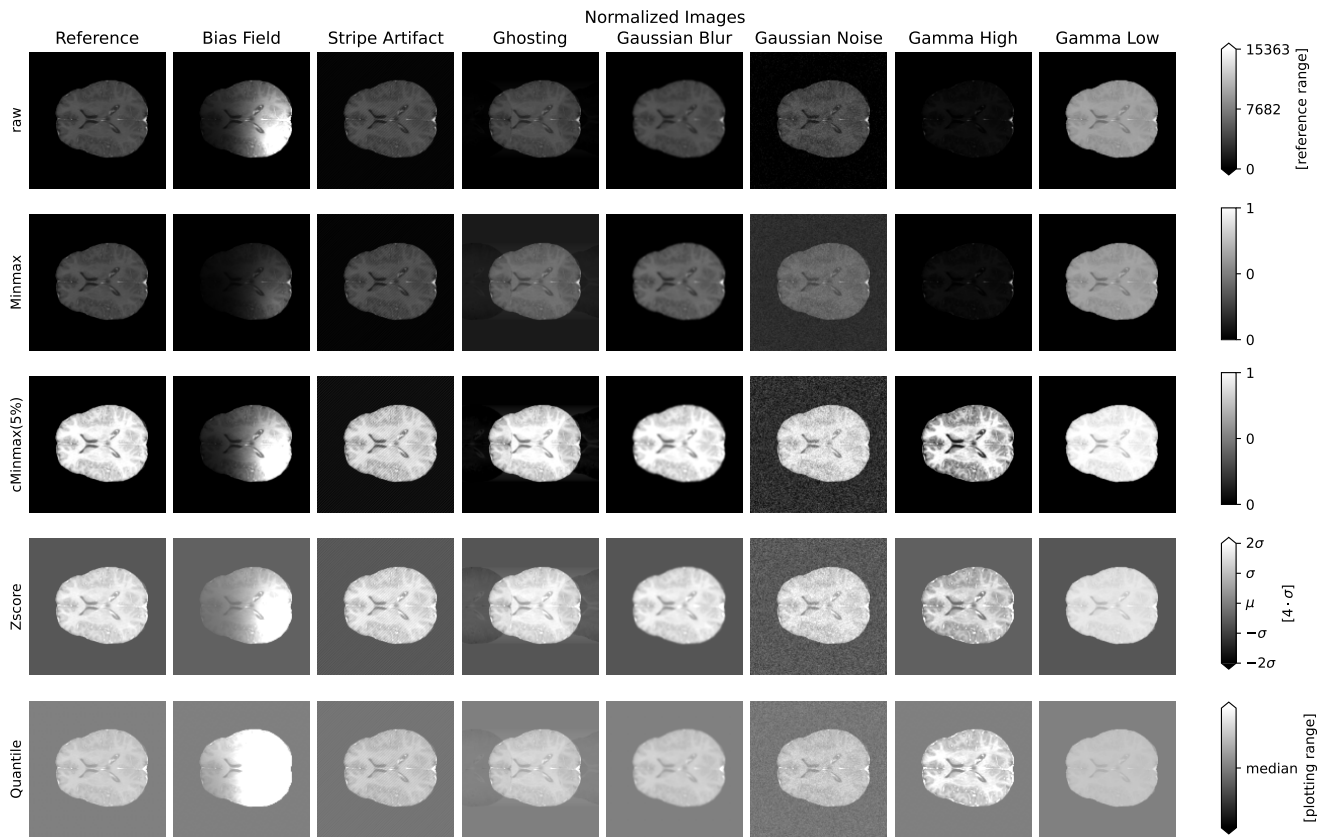


Figure A.2. Normalized reference and distorted images. In the first row, unnormalized raw reference image (first column) and different distortions applied with highest strength (5/5). The visualized range in the first row is restricted to the intensity range of the reference image. The second row, showing Minmax normalized images visualizes the full intensity range. Images normalized with cMinmax in the third row appear with higher contrast, because the intensity range is clipped at 5% and 95%. Zscore and Quantile yield similar result, but in these images, the mean is higher than the median, and the interquartile range (IQR) is smaller, than the standard deviation. Therefore, the Zscore normalized images appear darker in the background and with more contrast in the plotted intensity range $[-2, 2]$ compared to the Quantile normalized images, which appear brighter in the background and with less contrast in the plotted intensity range $[-2, 2]$.

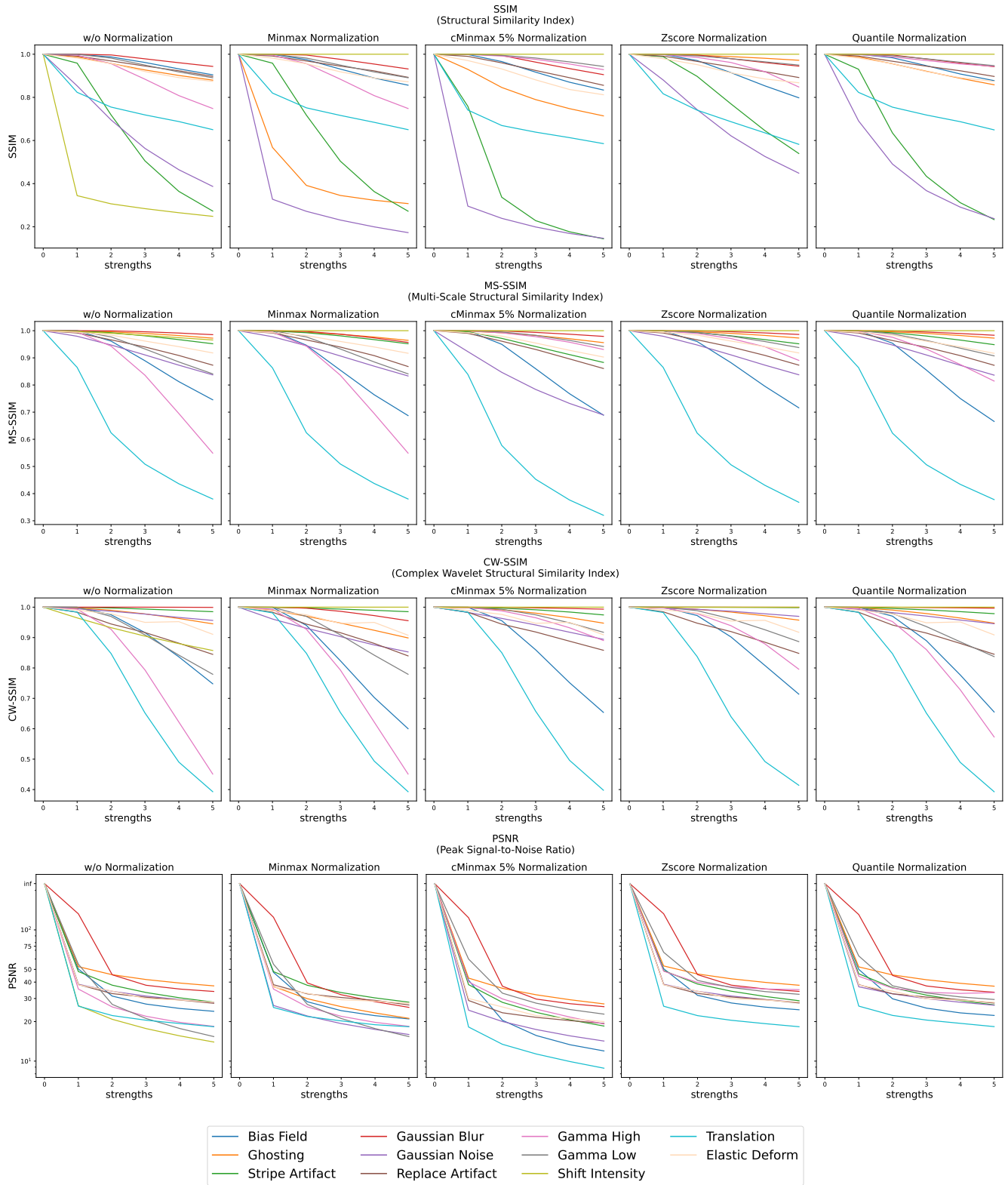


Figure A.3. Mean scores of SSIM-based reference metrics SSIM (top), MS-SSIM (second row), CW-SSIM (third row), and the PSNR metric (bottom) across 100 images, distorted with increasing strengths (0: reference, 1: hardly/not visibly distorted, 5: strongly distorted), grouped by kinds of distortions in different colors.

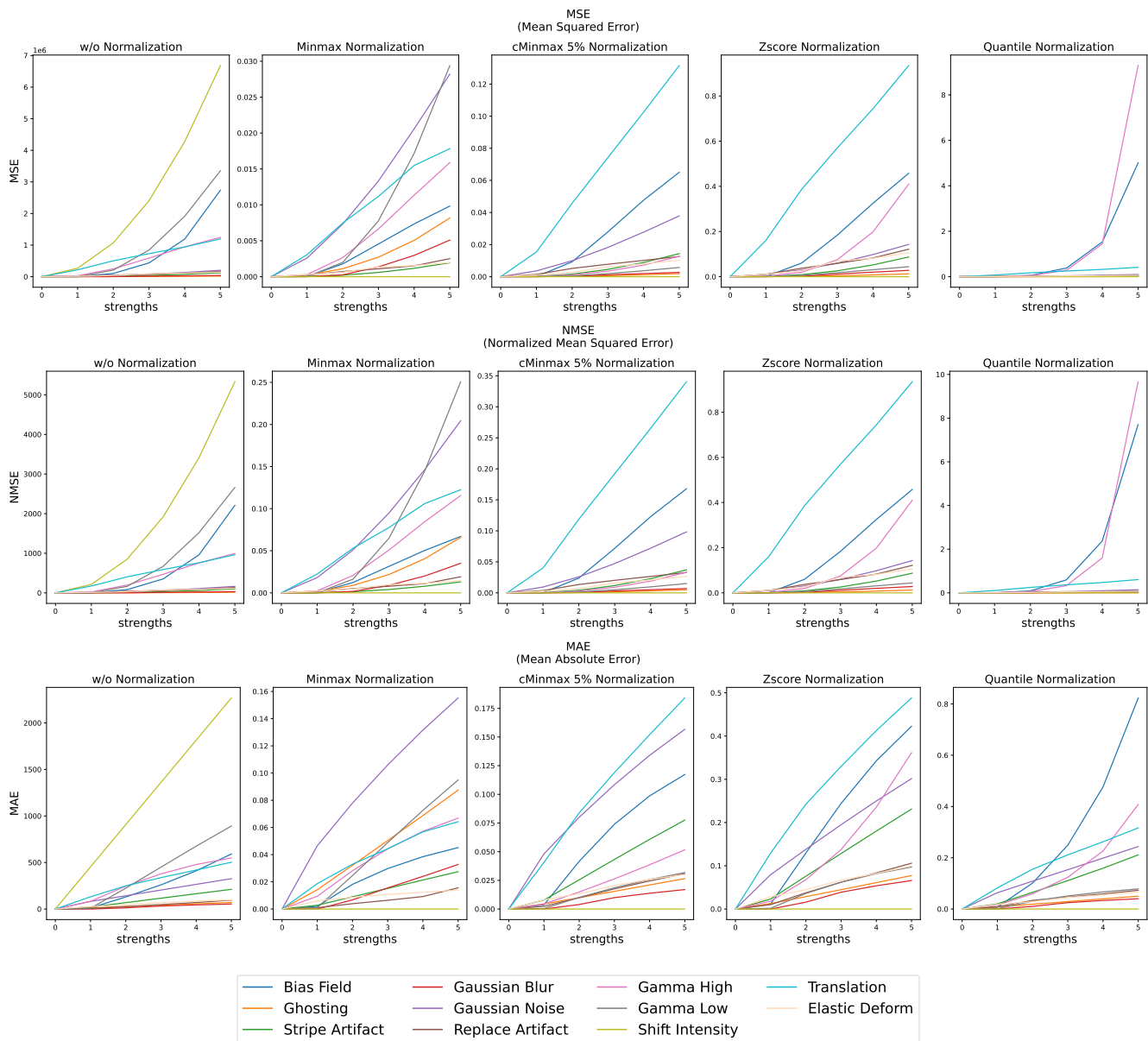


Figure A.4. Mean scores of error-based reference metrics MSE (top), NMSE (middle) and MAE (bottom) across 100 images, distorted with increasing strengths (0: reference, 1: hardly/not visibly distorted, 5: strongly distorted), grouped by kinds of distortions in different colors.

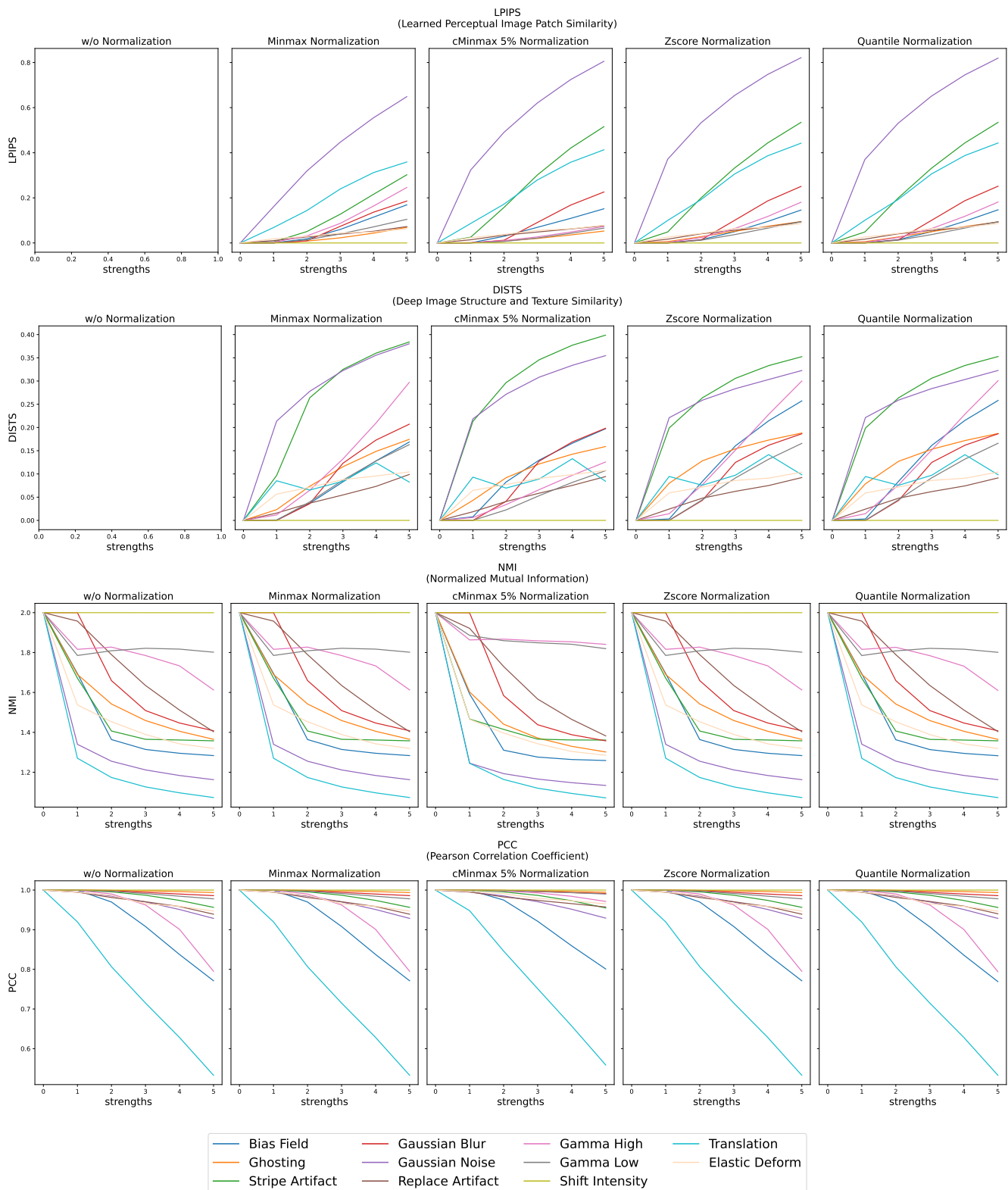


Figure A.5. Mean scores of the learned reference metrics LPIPS (top) and DISTs (second row), and statistical dependency reference metrics NMI (third row) and PCC (bottom) across 100 images, distorted with increasing strengths (0: reference, 1: hardly/not visibly distorted, 5: strongly distorted), grouped by kinds of distortions in different colors. LPIPS and DISTs require normalized images with an intensity range around 0, therefore, analysis of these metrics was not performed without normalization.

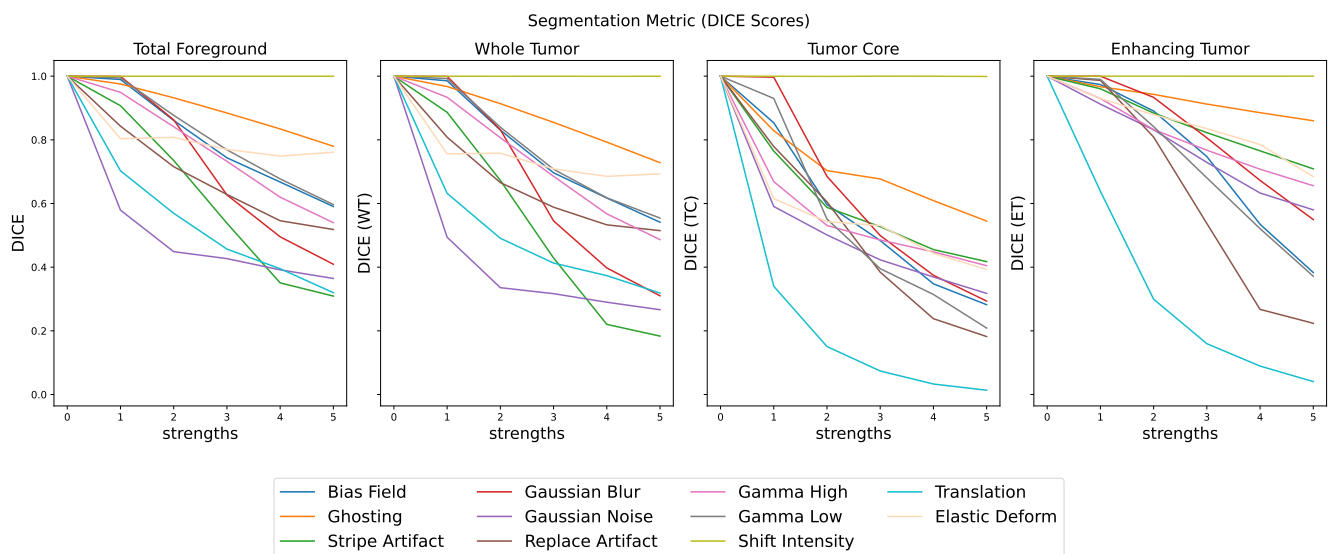


Figure A.6. Mean scores of the DICE segmentation metric across 100 segmentation pairs derived from a reference a distorted image with increasing strengths applied (0: reference, 1: hardly/not visibly distorted, 5: strongly distorted). The mean scores are grouped by kinds of distortions in different colors. The "Total Foreground" class includes the three disjoint classes "Whole Tumor" (mainly tumor surrounding edema), "Tumor Core" (mainly necrotic areas) and "Enhancing Tumor" (vital tumor cells, taking up contrast media).

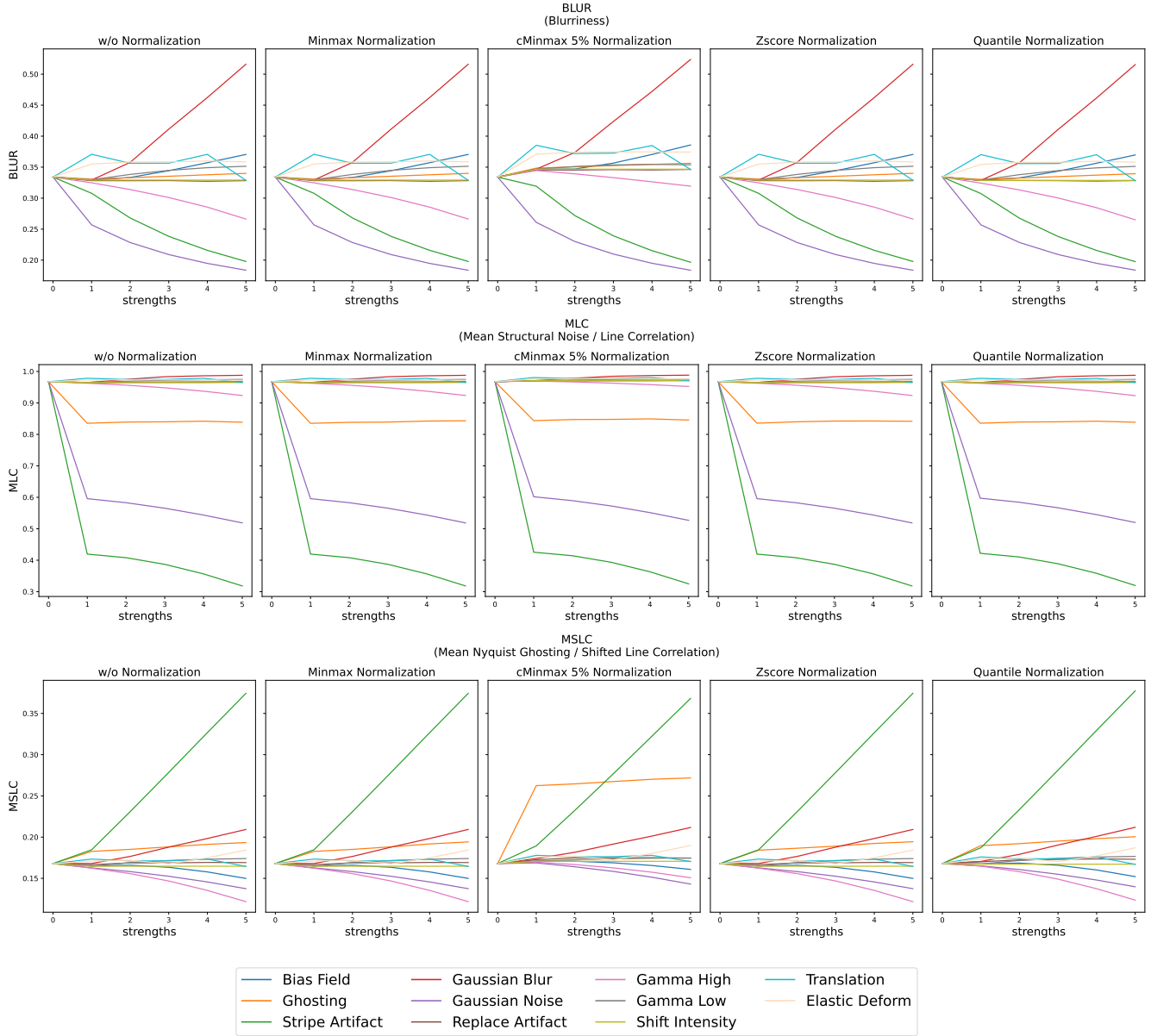


Figure A.7. Mean scores of the non-reference BLUR (top), MLC (middle), and MSLC (bottom) metric across 100 images, distorted with increasing strengths (0: reference, 1: hardly/not visibly distorted, 5: strongly distorted), grouped by kinds of distortions in different colors.